

# NUMERICAL SIMULATIONS OF TURBULENT MOLECULAR CLOUDS REGULATED BY REPROCESSED RADIATION FEEDBACK FROM NASCENT SUPER STAR CLUSTERS

M. AARON SKINNER AND EVE C. OSTRIKER

Department of Astrophysical Sciences, Princeton University, Princeton, NJ 08544-1001;  
 askinner@astro.princeton.edu, eco@astro.princeton.edu

*Draft version March 2, 2024*

## ABSTRACT

Radiation feedback from young star clusters embedded in giant molecular clouds (GMCs) is believed to be important to the control of star formation. For the most massive and dense clouds, including those in which super star clusters (SSCs) are born, pressure from reprocessed radiation exerted on dust grains may disperse a significant portion of the cloud mass back into the interstellar medium (ISM). Using our radiation hydrodynamics (RHD) code, *Hyperion*, we conduct a series of numerical simulations to test this idea. Our models follow the evolution of self-gravitating, strongly turbulent clouds in which collapsing regions are replaced by radiating sink particles representing stellar clusters. We evaluate the dependence of the star formation efficiency (SFE) on the size and mass of the cloud and  $\kappa$ , the opacity of the gas to infrared (IR) radiation. We find that the single most important parameter determining the evolutionary outcome is  $\kappa$ , with  $\kappa \gtrsim 15 \text{ cm}^2 \text{ g}^{-1}$  needed to disrupt clouds. For  $\kappa = 20 - 40 \text{ cm}^2 \text{ g}^{-1}$ , the resulting SFE = 50 – 70% is similar to empirical estimates for some SSC-forming clouds. The opacities required for GMC disruption likely apply only in dust-enriched environments. We find that the subgrid model approach of boosting the direct radiation force  $L/c$  by a “trapping factor” equal to a cloud’s mean IR optical depth can overestimate the true radiation force by factors of  $\sim 4 - 5$ . We conclude that feedback from reprocessed IR radiation alone is unlikely to significantly reduce star formation within GMCs unless their dust abundances or cluster light-to-mass ratios are enhanced.

**Keywords:** hydrodynamics – methods: numerical – radiation: dynamics – radiative transfer – ISM: clouds – stars: formation – galaxies: star clusters

## 1. INTRODUCTION

Giant molecular clouds (GMCs), the sites of star formation, form out of the diffuse interstellar medium (ISM) due to some combination of self-gravity, the gravity of the stellar disk and bulge (which compresses the ISM vertically everywhere and horizontally in spiral arms), and large-scale gas motions associated with turbulence, supernova remnant or superbubble expansion, and other ISM flows (e.g., McKee & Ostriker 2007; Dobbs et al. 2014). However, GMCs are not believed to be permanent structures, and based on age-dating of associated star clusters (in the Milky Way and other galaxies) are thought to survive for at most several internal free-fall times (Leisawitz et al. 1989; Kawamura et al. 2009; Miura et al. 2012; Whitmore et al. 2014). It is widely believed that “feedback” from massive stars is responsible for the demise of GMCs, but exactly how this works is still poorly understood. Among the most basic uncertainties is which among the possible feedback effects predominate for different regimes of GMC properties and surrounding environment. Currently, the most-discussed candidate effects (see, e.g., the review of Krumholz et al. 2014) include (1) (magneto)hydrodynamic forces from overpressured regions produced by ionizing radiation, shocked stellar winds, or supernova blasts; and (2) radiation forces from the primary absorption of stellar optical and ultraviolet (UV), and from the secondary absorption of reprocessed infrared (IR).

Both theoretical and observational motivations have led to an increased interest in the effects of radiation forces. Although supernovae inject an order of magni-

tude more momentum per stellar mass to their surroundings than other forms of feedback (Ostriker & Shetty 2011; Kim & Ostriker 2015; Iffrig & Hennebelle 2015; Walch & Naab 2014; Martizzi et al. 2015; Geen et al. 2015), there is a significant time delay between the advent of star formation in a GMC and the explosion of the first supernova (and further delay before the last massive stars die). If other agents are able to destroy the GMC in this interval, much of the momentum and energy from supernovae (SNe) may be delivered to the diffuse ISM rather than the progenitor’s birth cloud.

In GMCs with low escape speeds hosting clusters containing massive stars, the combination of photoevaporation and the pressure force from the expanding H II region can unbind much of a cloud’s initial mass (e.g., Matzner 2002; Dale et al. 2012, 2013, and references therein). However, analytic spherical models (Krumholz & Matzner 2009; Murray et al. 2010; Fall et al. 2010) of clusters within clouds suggest that the effects from radiation pressure will exceed that from ionized gas pressure at high values of the total cloud mass and surface density. Furthermore, the relative importance of reprocessed IR compared to direct optical/UV is expected to increase as the cloud surface density increases. Observational evidence suggests that radiation pressure exceeds ionized gas pressure close to the centers of H II regions around massive clusters (consistent with the theory of Draine 2011a), and for younger systems (Lopez et al. 2011, 2014; Pellegrini et al. 2007). Although historically the gas pressure from shocked stellar winds was expected to drive dynamics around massive clusters at early times, this has

been called into question for some systems due to the lack of X-ray emission, with the suggestion that the primary wind and/or hot shocked gas largely escapes (Townsend et al. 2003; Harper-Clark & Murray 2009; Rogers & Pittard 2013).

Embedded super star clusters (SSCs) in dense GMCs represent the systems for which radiation pressure is expected to play the greatest role. Considering that they are still deeply buried in GMCs, the primary signature of these SSCs is thermal radio emission, indicating clusters of masses  $\sim 10^4 - 10^6 M_\odot$  powering H II regions only a few pc in size (Turner et al. 1998, 2000; Kobulnicky & Johnson 1999; Johnson et al. 2001; Johnson & Kobulnicky 2003; Johnson et al. 2015; Reines et al. 2008; Tsai et al. 2009; Kepley et al. 2014). The molecular clouds associated with these SSCs are far denser than typical Milky Way GMCs. For example, “Cloud D” in NGC 5253 has a mass  $\sim 2 \times 10^6 M_\odot$  and diameter  $\sim 40$  pc based on the SMA observations of Turner et al. (2015), giving a mean density of hydrogen nuclei  $n_H = 1800 \text{ cm}^{-3}$  and mean surface density  $\Sigma = 1600 M_\odot \text{ pc}^{-2} = 0.33 \text{ g cm}^{-2}$ . The “pre-SSC” cloud in the Antennae system studied with ALMA by Johnson et al. (2015) has an estimated mass  $\sim 0.3 - 1.5 \times 10^7 M_\odot$  and diameter  $< 40$  pc, yielding  $n_H \gtrsim 0.26 - 1.3 \times 10^4 \text{ cm}^{-3}$  and  $\Sigma \gtrsim 0.2 - 1.2 \times 10^4 M_\odot \text{ pc}^{-2}$ . In the central starburst region of NGC 253, ALMA observations of high critical density tracers by Leroy et al. (2015) identified clouds with radii  $10 - 50$  pc and masses  $0.2 - 6 \times 10^7 M_\odot$ , implying typical  $n_H \sim 2000 \text{ cm}^{-3}$  and  $\Sigma \sim 6000 M_\odot \text{ pc}^{-2}$ .

The deeply embedded nature of SSCs makes it difficult to constrain the relative importance of different feedback mechanisms empirically. However, the SFEs appear to be at least an order of magnitude higher than in typical Milky Way GMCs (e.g., Tsai et al. 2009). The young, isolated Cloud D in NGC 5253 has an estimated star formation efficiency (SFE)  $\sim 0.6$ , well above the range  $\sim 0.01 - 0.2$  estimated for the most luminous Milky Way star-forming complexes (Murray 2011). It is clearly of interest to develop theoretical models that explore the effects of feedback in controlling star formation and setting SFEs in GMCs comparable to SSC hosts. This may also inform our understanding of globular cluster formation, which presumably occurred in similarly dense and massive clouds.

Because forces from reprocessed IR radiation become increasingly important as gas surface densities increase,<sup>1</sup> the pressure from trapped IR has been argued to dominate the regulation of star formation in the most extreme systems (Thompson et al. 2005; Murray et al. 2010). However, analytic models typically require major simplifications to be tractable (including having all the gas mass collected in a thin, uniform-density spherical shell, and having a single stellar cluster that is centrally located with a luminosity that is fixed in time), and it is unclear the extent to which these may affect the conclusions. It is therefore useful to employ time-dependent numerical simulations to investigate systems with more structural

and temporal complexity.

In this paper, we shall consider numerical models of massive, compact, turbulent GMCs that fragment gravitationally to form massive star clusters. Our model clouds have surface density  $1600 - 6200 M_\odot \text{ pc}^{-2}$ , comparable to the GMCs in starburst nuclei within which SSCs are born. Optical and UV radiation from young, hot stars dominate the luminosity of massive clusters, but these primary photons are likely to be absorbed by dust very near their source. This warm dust then radiates isotropically into the lower-frequency IR band, which has a much smaller absorption cross-section but can still be absorbed and re-emitted multiple times in high-column GMCs.

In our simulations, we apply radiation hydrodynamics (RHD) methods to focus on the effects of long-wavelength radiation. We consider the regime of clouds at relatively high mass and density, such that the optical depth to IR exceeds unity and simple spherical models would predict that the radiation force from reprocessed IR exceeds that of the direct optical/UV. We follow the co-evolution of the gas and radiation in the system, under the assumption that radiation forces applied to dust are transferred to the gas (i.e., assuming perfect gas-dust collisional coupling), and that all radiation that is absorbed is locally re-emitted. Over time, the fraction of a cloud’s mass converted to stars increases as more and more gas collapses. However, as the stellar luminosity grows, the radiation field exerts increasing outward forces on the gas. Under certain conditions, we show that a significant portion of the cloud’s initial gas mass is expelled from the system.

Our models are highly idealized, in that we consider exclusively the effects of long-wavelength radiation, with spatially-uniform opacity. As our numerical code presently allows only a single opacity, here we do not consider the direct effects of either ionizing or non-ionizing UV; effectively, we treat radiation as being degraded to IR close to each stellar cluster source. In reality, several feedback effects operate simultaneously, and complete models must eventually include (at least) non-ionizing as well as ionizing UV, and stellar winds. The present set of simulations provides a baseline for more comprehensive studies, similar to the baseline provided by simulations that focus exclusively on the effects of ionizing radiation and cloud disruption from H II region expansion (e.g., Dale et al. 2012, 2013; Walch et al. 2012).

We note that all of our clouds have escape speeds exceeding  $20 \text{ km s}^{-1}$ . In this regime, the simulations of Dale et al. (2012, 2013) suggest that photoevaporation combined with the pressure from ionized gas would be able to unbind no more than 1% of the cloud’s mass prior to the advent of supernovae. Additionally, although realistic RHD models focused on non-ionizing UV radiation have not yet been completed for this extreme regime (very high  $\Sigma$  and large  $v_{\text{esc}}$ ), analytic models have been developed that account for the effects of turbulence-driven internal structure in the radiation/gas interaction (Thompson & Krumholz 2014; Raskutti, Ostriker, & Skinner 2015, in preparation); the Raskutti et al model has also been verified via numerical RHD simulations in the lower- $\Sigma$  regime. These models predict that it would be difficult for the direct UV radiation to expell substantial material from large, dense GMCs, since

<sup>1</sup> For the spherical case, the total force imparted to the gas is  $(1 + \tau_{\text{IR}})L_*/c$  where  $L_*$  is the stellar luminosity and  $\tau_{\text{IR}}$  is the center-to-edge IR optical depth, proportional to the cloud’s surface density.

the already-high mean surface density is increased in the filamentary structures that comprise most of the cloud’s mass. Thus, as prior studies suggest that neither ionizing or non-ionizing UV will be effective in destroying GMCs for the cloud regime studied here, we are motivated to turn the focus to the effects of reprocessed IR. To our knowledge, this work represents the first direct RHD study of the dynamical effects of reprocessed radiation in turbulent, self-gravitating, star-forming clouds.

The plan of this paper is as follows. We begin with a summary of our numerical methods, model specification, and model parameters, together with tests to verify code performance (Section 2). We then consider evolution of a fiducial model (Section 3.1), which also serves to illustrate the radiation structure and differences in the radiation/matter interaction compared to simple spherical systems (Section 3.2). In Section 3.3, we analyze the effects of varying the opacity, demonstrating that quite high opacity ( $\kappa > 10 \text{ cm}^2 \text{ g}^{-1}$ ) is required for substantial mass to be ejected by radiation forces; we also quantify the gas-radiation anticorrelation and the level of radiation trapping. Our set of simulations allows for varying cloud mass and radius as well as a range of opacity; Section 3.4 compares simulation outcomes (including net SFE and net momentum ejected) for different model parameters. Section 4 summarizes and discusses our conclusions.

## 2. NUMERICAL METHODS & MODEL DESCRIPTIONS

### 2.1. Numerical Methods

We evolve the equations of RHD using our Godunov code *Hyperion* (Skinner & Ostriker 2013, hereafter SO13). *Hyperion* is an extension of the *Athena* code (Stone et al. 2008) for computational hydrodynamics and magnetohydrodynamics (MHD); we employ the van Leer algorithm of Stone & Gardiner (2009) to integrate the gas equations, utilizing the HLLC Riemann solver and a piecewise-linear spatial reconstruction scheme. For simplicity in this first study, we neglect magnetic fields and adopt an isothermal equation of state (EOS); as the sound speed is small compared to other speeds in the problem, the dynamics are insensitive to its exact value. Gravity of the gas as well as the “star particles” (representing collapsed regions that have formed star clusters) is computed via Fourier methods, as described below.

In *Hyperion*, the radiation energy density and flux, i.e., the zeroth and first moments of the radiation intensity, are advanced in time using a piecewise-linear spatial reconstruction and an HLL-type Riemann solver. For the radiation energy equation, we adopt the limit of radiative equilibrium, such that all absorbed radiation is re-emitted locally. For long wavelength radiation, which we consider, scattering is small compared to true absorption and is neglected in our treatment. As velocities are small compared to the speed of light and optical depths are moderate, we adopt the static diffusion limit in which terms of  $\mathcal{O}(v/c)$  and  $\mathcal{O}(\tau v/c)$  are neglected. Finally, we employ the reduced speed of light approximation (RSLA) (Gnedin & Abel 2001), which allows us to solve the radiation subsystem explicitly rather than implicitly (see also Rosdahl et al. 2013). The only sources of radiation are the star particles.

The system of equations to be solved for the gas and

radiation is given by

$$\partial_t \rho + \nabla \cdot (\rho \mathbf{v}) = 0, \quad (1a)$$

$$\partial_t (\rho \mathbf{v}) + \nabla \cdot (\rho \mathbf{v} \mathbf{v} + P \mathbb{I}) = -\rho \nabla \Phi + \rho \kappa \frac{\mathbf{F}}{c}, \quad (1b)$$

$$\frac{1}{\hat{c}} \partial_t \mathcal{E} + \nabla \cdot \left( \frac{\mathbf{F}}{c} \right) = \frac{j_*}{c}, \quad (1c)$$

$$\frac{1}{\hat{c}} \partial_t \left( \frac{\mathbf{F}}{c} \right) + \nabla \cdot \mathbb{P} = -\rho \kappa \frac{\mathbf{F}}{c}, \quad (1d)$$

where  $\rho$ ,  $\mathbf{v}$ , and  $P$  are the gas density, velocity, and pressure, respectively, and  $\Phi$  is the gravitational potential. In Equations (1),  $\mathcal{E}$ ,  $\mathbf{F}$ , and  $\mathbb{P}$  are the frequency-integrated radiation energy density, flux vector, and pressure tensor, respectively, which are measured in the inertial frame, and  $\hat{c}$  is the reduced speed of light. The absorption opacity,  $\kappa$ , is taken to be a spatial constant, although we vary this parameter in different models. Finally, the term  $j_*$  in Equation (1c) represents emission of radiation from star particles.

The *Hyperion* code uses the  $M_1$  closure relation (Levermore & Pomraning 1981; González et al. 2007) to express  $\mathbb{P}$  as a function of  $\mathcal{E}$  and  $\mathbf{F}$  in Equations (1). The radiation subsystem in Equations (1c) and (1d) is operator-split from the gas subsystem in Equations (1a) and (1b) and is explicitly evolved by subcycling on a time step determined by the radiation propagation speed,  $\hat{c}$ . Using the RSLA, we choose  $\hat{c}$  satisfying the RSLA static diffusion criterion (SO13),

$$\hat{c} \gg v_{\max} \max\{1, \tau_{\max}\}, \quad (2)$$

where  $v_{\max}$  is the maximum velocity of the gas and  $\tau_{\max}$  is the maximum optical depth in the simulation. This allows us to reduce the radiation-to-gas time step ratio to a reasonable level, but has a negligible effect on the system’s dynamics as the gas evolves much more slowly than the radiation field. Our simulations typically use a value of  $\hat{c}$  such that  $\hat{c}/v_{\max} \sim 10 - 100$ , which is substantially less than realistic values of  $c/v_{\max} \sim 10^4 - 10^5$ , making explicit time integration computationally feasible.

In *Hyperion*, star particles are treated using the algorithm developed by Gong & Ostriker (2013), with added functionality to provide for the luminosity of the particles.<sup>2</sup> The  $M_1$  closure cannot resolve the behavior of a streaming radiation field too near to a true point source, since the radiation flux from such a source varies rapidly in angle. Therefore, radiation sources in our algorithm must be resolved over some minimum number of grid zones. We have found it convenient to add radiation energy density to the grid using a Gaussian source function given by

$$j_*(\mathbf{x}) = \frac{L_*}{(2\pi\sigma_*^2)^{3/2}} \exp\left(-\frac{|\mathbf{x} - \mathbf{x}_*|^2}{2\sigma_*^2}\right), \quad (3)$$

where  $L_*$  is the star particle’s luminosity,  $\mathbf{x}_*$  is the star particle’s position, and  $\sigma_* \equiv R_*/\sqrt{2 \ln 2}$  is set such that the half-width at half-maximum (HWHM) of the distribution is equal to the star particle’s effective size,  $R_*$ . Note that  $\int_0^r j_*(r') 4\pi r'^2 dr' \rightarrow L_*$  for  $r/R_* \gg 1$ . In

<sup>2</sup> At the resolution of our simulations, each “star particle” actually represents a fully-sampled star cluster.

practice, we have found that sources with  $R_*/\Delta x \gtrsim 8$  are sufficiently well-resolved that angular variations in the radiation flux at radii  $r \gg R_*$  are negligible (see Section 2.2).

To compute gravitational forces including contributions from both gas and star particles, we first use the particle mesh (PM) method to assign the star particle masses to a discrete grid via the triangular-shaped cloud (TSC) method, as described in Gong & Ostriker (2013). We then apply the “zero-padding” method of Hockney & Eastwood (1988) to obtain the potential,  $\Phi(\mathbf{x})$ , of an isolated source distribution subject to open (vacuum) boundary conditions via fast Fourier transforms (FFTs). This potential is given by the solution of Poisson’s equation,

$$\nabla^2 \Phi = 4\pi G \rho(\mathbf{x}), \quad (4)$$

for a given density field,  $\rho(\mathbf{x})$ ;  $\rho$  includes both contributions from the gas and the star particles. Solutions of Equation (4) can be expressed as the convolution

$$\Phi(\mathbf{x}) = G \int \mathcal{G}(\mathbf{x}, \mathbf{x}') \rho(\mathbf{x}') d^3 \mathbf{x}', \quad (5)$$

where  $\mathcal{G}(\mathbf{x}, \mathbf{x}') = \mathcal{G}(|\mathbf{x} - \mathbf{x}'|) = -|\mathbf{x} - \mathbf{x}'|^{-1}$  is a Green function solution of the equation  $\nabla^2 \mathcal{G} = 4\pi \delta^3(\mathbf{x} - \mathbf{x}')$ . Using the Fourier convolution theorem, Equation (5) may be re-expressed as the convolution of the Fourier transforms of the density distribution and Green function; details of this are given in the Appendix.

## 2.2. Model Description

Each model cloud is initiated as a uniform-density sphere of radius  $R_{\text{cloud}}$  and mass  $M_{\text{cloud}}$ . The cloud is centered in a computational box of side length  $L_{\text{box}} = 4R_{\text{cloud}}$  with background density set to 1% of the initial cloud density.<sup>3</sup> A highly supersonic turbulent velocity field is applied initially, which rapidly creates density structure within the cloud. Over time, this initial velocity field decays, although collapse and radiation forces drive further turbulent motions.

We initialize the turbulent velocity field using Gaussian random perturbations with power spectrum  $|\delta \mathbf{v}| \propto k^{-4}$ , for  $k/dk \in [2, 64]$ , where  $dk = 2\pi/L_{\text{box}}$ , as described in Stone et al. (1998). The velocity perturbations are normalized such that  $\alpha_{\text{vir,init}} = 2$ , corresponding to a just-bound state, where

$$\alpha_{\text{vir}} \equiv 2 \frac{E_{\text{kin}}}{E_{\text{grav}}} \quad (6)$$

is the virial parameter, and where  $E_{\text{kin}} = (1/2)M_{\text{cloud}}\sigma^2$  and  $E_{\text{grav}} = (3/5)GM_{\text{cloud}}^2/R_{\text{cloud}}$  are the initial kinetic and gravitational energies of the gas, respectively;  $\sigma = [\alpha_{\text{vir,init}} 3GM_{\text{cloud}}/(5R_{\text{cloud}})]$  is the initial turbulent velocity dispersion.<sup>4</sup> The velocities of the perturbations are recentered such that they add no net momentum to the computational domain, i.e., such that  $\int \rho \delta \mathbf{v} dV = 0$ .

<sup>3</sup> Realistic clouds may have lower density contrast relative to their surroundings, which could lead to additional late-time accretion. However, for this first study we consider isolated clouds for simplicity.

<sup>4</sup> Note that for a uniformly dense sphere, such as our initial configuration,  $\alpha_{\text{vir}}$  is equivalent to the often-used definition of the virial parameter from Bertoldi & McKee (1992, see Equation 2.8a).

For all simulations, the isothermal sound speed is set to  $c_s = 2 \text{ km s}^{-1}$ . We adopt this value, somewhat larger than true thermal sound speeds in cold clouds, in part to limit extreme shock compression, as would occur if we had included magnetic fields. We have found that results are insensitive to the exact choice of the sound speed, provided the Mach number is large. The initial turbulent Mach number is  $\sim 11$  for our fiducial parameters (see below), and more generally the turbulent flows in all of our models are highly supersonic. Tests show that there is little variation in simulation outcomes for different realizations of the initial random perturbed velocity field (see Section 3.1), so we use a single realization for most sets of model parameters.

Following Gong & Ostriker (2013), the density threshold for star particle creation is set using the Larson-Penston criterion,  $\rho_{\text{thr}} = \rho_{\text{LP}}(r = \Delta x/2)$ , where

$$\rho_{\text{LP}}(r) = \frac{8.86 c_s^2}{4\pi G r^2} \quad (7)$$

describes the density profile of the asymptotic state produced by gravitational collapse of an isothermal sphere (Larson 1969; Penston 1969); this profile is approached for collapse initiated from a wide variety of initial conditions, including supersonic turbulent flows (see Gong & Ostriker 2009, 2011). As discussed in Gong & Ostriker (2013), the Larson-Penston density criterion is a factor of  $\sim 14$  times larger than the Truelove criterion (Truelove et al. 1997) used in many other star particle creation implementations (see, e.g., Krumholz et al. 2004; Federrath & Klessen 2012), but the star particles produced in a turbulent flow follow essentially the same histories.

We assume the star clusters that form in the cloud (represented as star particles) have a bolometric luminosity per unit mass of  $\Psi = 1700 \text{ erg s}^{-1} \text{ g}^{-1}$ , as obtained from a Starburst99 model (Leitherer et al. 1999) for the total luminosity of a young cluster that fully samples a Kroupa initial mass function (IMF), averaged over a lifetime of 5 Myr.<sup>5</sup> Since the total luminosity of a cluster would not change substantially over the cloud’s lifetime, for simplicity we set  $L_* = \Psi M_*$ , independent of the star particle’s age.

We adopt a constant effective physical size for each star particle, which we take to be  $R_* = 1 \text{ pc}$ . Sources of this size are generally consistent with observations of young, embedded super-star clusters (e.g., Johnson & Kobulnicky 2003) as well as older clusters (Murray 2009). Note that here, we do not attempt to model the H II region that those star clusters would create. For high luminosity sources, UV radiation pressure on dust significantly alters the conditions within H II regions compared to the classical Strömgren solution (Binette et al. 1997; Dopita et al. 2002; Draine 2011a), with radiation forces strongly compressing the photoionized gas. In principle, high pressure from a shocked stellar wind could further

<sup>5</sup> For random sampling of a fixed IMF,  $\Psi$  saturates for clusters of mass  $M_{\text{cl}} \gtrsim 10^4 M_{\odot}$ . In our simulations, we find that star particles, which represent star clusters on the scales we consider, may occasionally form with masses of order a few times less than  $10^4 M_{\odot}$ . However, these somewhat under-sampled clusters typically comprise a trivial fraction of the total mass in stars, which is dominated by fully-sampled clusters. Furthermore, these lower-mass star particles tend to accrete sufficient gas over a short enough time scale to justify the use of a constant specific luminosity.

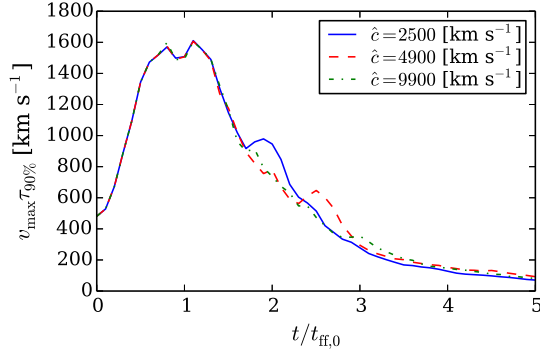


**Figure 1.** Time evolution of  $v_{\max}\tau_{90\%}$  for three different values of the reduced speed of light,  $\hat{c}$ , where  $v_{\max} \equiv \sigma + c_s$  approximates the maximum hydrodynamic signal speed and  $\tau_{90\%}$  is the optical depth at the 90th percentile over all projections of the grid in all directions. All runs were performed with  $N = 128^3$  zones. This demonstrates that the time evolution of the optical depth for the bulk of the gas is insensitive to the actual value of the reduced speed of light used, provided the RSLA static diffusion criterion of Equation (2) is satisfied. The value of  $\hat{c} = 4900 \text{ km s}^{-1}$  is the reduced speed of light in our fiducial run.

compress the photoionized gas, but observed ionization parameter measures suggest that this does not occur in practice (Yeh & Matzner 2012). Given the uncertainties about the effective size of the emission region in which the cluster’s radiation is reprocessed into IR, we opt to keep  $R_*$  fixed rather than having it depend on the mass and age of each star particle. Tests indicate that varying the physical size  $R_*$  of each star particle radiation source by a factor of two in either direction at fixed grid resolution only affects the final total mass in stars by about 5% (see Section 3.1).

From Equation (2), the required value of  $\hat{c}$  depends on the maximum optical depth and velocity in the model. If we define  $\tau_{90\%}$  at a given time as the optical depth at the 90th percentile over all projections of the grid in all directions, our tests show that the maximum of  $\tau_{90\%}$  over a simulation run is comparable to  $\tau$ , the initial IR optical depth across the GMC, within a factor of a few, and that this value is well-converged if we use  $\hat{c} = 5v_{\max}\tau$ . Figure 1 shows the time evolution of  $v_{\max}\tau_{90\%}$  for three different values of  $\hat{c}$ , where  $v_{\max} = \sigma + c_s$  approximates the maximum hydrodynamic signal speed. Each of these runs was performed at a reduced resolution of  $N = 128^3$  zones for parameters otherwise the same as the fiducial model (K20), and the choices of 2500, 4900, and 9900  $\text{km s}^{-1}$  for  $\hat{c}$  correspond to 5, 10, and 20 times  $(\sigma + c_s)\tau$ , respectively. The data clearly indicate that the optical depth that is “seen” by the majority of the radiation is insensitive to the specific value of  $\hat{c}$ , provided the RSLA static diffusion criterion of Equation (2) is satisfied. In all of our simulations, we therefore choose  $\hat{c}$  such that  $\hat{c} \geq 5(\sigma + c_s)\tau$ ; in most simulations we have  $\hat{c} = 10(\sigma + c_s)\tau$ .

In our current investigation, which focuses on effects of reprocessed radiation that is absorbed and re-emitted by dust, the absorption opacity of the medium,  $\kappa$ , is taken to be a constant in space and time. More realistically, the opacity law would depend on the frequency of the radiation as well as on local dust abundance and properties, such that the frequency-averaged opacity would depend on these properties and also the particular radiation regime. For example, consider the energy-, Planck-,

flux-, and Rosseland-mean opacities, which are defined, respectively, by

$$\kappa_{\mathcal{E}} \equiv \frac{\int \kappa_{\nu} \mathcal{E}_{\nu} d\nu}{\int \mathcal{E}_{\nu} d\nu}, \quad (8a)$$

$$\kappa_{\mathcal{P}} \equiv \frac{\int \kappa_{\nu} B_{\nu} d\nu}{\int B_{\nu} d\nu}, \quad (8b)$$

$$\kappa_F \equiv \frac{\int \kappa_{\nu} F_{\nu} d\nu}{\int F_{\nu} d\nu}, \quad (8c)$$

$$\kappa_R \equiv \frac{\int \partial B_{\nu} / \partial T d\nu}{\int \kappa_{\nu}^{-1} (\partial B_{\nu} / \partial T) d\nu}. \quad (8d)$$

For an optically thick flow, if we assume the radiation field is that of a blackbody, then  $\kappa_{\mathcal{E}} = \kappa_{\mathcal{P}}$  and  $\kappa_F = \kappa_R$ . In contrast, for an optically thin flow, since  $F_{\nu} \propto \mathcal{E}_{\nu}$ , it follows that  $\kappa_F = \kappa_{\mathcal{E}}$ . However, the assumption that the radiation field is a blackbody is dubious in this regime, hence it is unclear whether or not  $\kappa_{\mathcal{E}}$  and  $\kappa_{\mathcal{P}}$  are even related. A full frequency-dependent treatment of radiation would require some transition between optically thick and thin regimes. Here, the primary interest is investigating the effects of radiation forces that develop under optically thick conditions, such that the most relevant single value of the opacity is  $\kappa_F = \kappa_R$ . For temperatures  $\lesssim 100 \text{ K}$ , the frequency dependence of  $\kappa_{\nu} \propto \nu^2$  leads to an approximate dependence  $\kappa_R \propto T^2$  (Draine 2011b), and some recent simulations investigating radiation in dusty starburst disks have included this dependence (Krumholz & Thompson 2012; Davis et al. 2014). For the moderate optical depth as would apply in molecular clouds of surface density  $\sim 1 \text{ g cm}^{-2}$ , the opacity would increase by less than a factor  $\sim 2$  from the edge to the center of the cloud, and for simplicity we adopt a constant  $\kappa$ . We allow, however, for a range of values of  $\kappa$ , as described below.

We consider four series of runs over a wide range of GMC conditions, which we summarize in Table 1. Our model parameters are the adopted opacity,  $\kappa$ , and the initial cloud radius and mass,  $R_{\text{cloud}}$  and  $M_{\text{cloud}}$ , respectively. In addition to the basic input parameters, for each model Table 1 lists the initial gas surface density,  $\Sigma \equiv M_{\text{cloud}}/(\pi R_{\text{cloud}}^2)$ , the initial turbulent velocity dispersion,  $\sigma$ , the initial optical depth through the cloud, and the initial free-fall time of the cloud,  $\tau t_{\text{ff}} \equiv [\pi^2 R_{\text{cloud}}^3 / (8GM_{\text{cloud}})]^{1/2}$ . We run each simulation for 8 times the initial free-fall time, i.e., to  $t_{\text{final}} = 8 t_{\text{ff}}$ .

In the K series, we vary the opacity while holding  $R_{\text{cloud}} = 10 \text{ pc}$  and  $M_{\text{cloud}} = 10^6 M_{\odot}$  fixed, which allows  $\tau$  to vary while  $\Sigma$  and  $\sigma$  do not. As we shall discuss in Section 3.2, simple scaling arguments suggest that the most important parameter in determining the fate of a cloud with feedback dominated by IR radiation is  $f_{\text{Edd},*} \equiv \kappa\Psi/(4\pi cG)$ ; the K series allows us to focus on this dependence. For gas-to-dust ratio  $\sim 100$ , realistic values of the Rosseland mean opacity for reprocessed IR radiation are likely in the range  $\kappa \sim 1 - 5 \text{ cm}^2 \text{ g}^{-1}$  (Semenov et al. 2003), but we include a much larger range  $\kappa = 1 - 40 \text{ cm}^2 \text{ g}^{-1}$  in the K series to explore the physical dependence of the results on  $\kappa$ . The values at the upper end of the opacity range in our models may apply for ISM regions that have high dust abundances. Potentially, GMCs with high SFE may have dust abundances

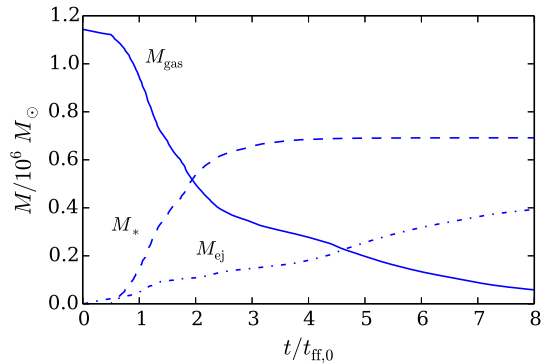


**Figure 2.** Evolutionary history of the fiducial model, with  $\kappa = 20 \text{ cm}^2 \text{ g}^{-1}$ ,  $R_{\text{cloud}} = 10 \text{ pc}$ , and  $M_{\text{cloud}} = 10^6 M_{\odot}$  (see K20 in Table 1). Shown are the gas mass within the domain (including the diffuse background gas, which is initially set to 1% of the initial cloud density), the mass that has been ejected from the box, and the total mass in star particles. Time is in units of the initial free-fall time within the cloud.

enhanced by self-enrichment. As discussed in Section 1, with  $\tau \geq 1$  in all runs we expect the reprocessed IR radiation force to dominate over the direct radiation force. Also, since  $\sigma \geq 16 \text{ km s}^{-1}$ , which exceeds the maximum expansion velocity of  $\sim 10 \text{ km s}^{-1}$  for H II regions, we would not expect significant contribution from H II pressure for clouds in the regime under investigation.

In the R series, we vary  $R_{\text{cloud}}$  while holding  $M_{\text{cloud}} = 10^6 M_{\odot}$  fixed, while in the M series, we vary the cloud mass,  $M_{\text{cloud}}$ , while holding the cloud radius  $R_{\text{cloud}} = 10 \text{ pc}$  fixed. In both the R and M series, we hold  $\kappa$  fixed, but  $\Sigma$ ,  $\sigma$ , and  $\tau$  all depend on both the cloud radius and mass, hence vary with either of them, albeit in different ways. Finally, in the RM series, we vary both  $R_{\text{cloud}}$  and  $M_{\text{cloud}}$  together such that  $M_{\text{cloud}} \propto R_{\text{cloud}}^2$ , while holding  $\kappa$  fixed. Thus, in the RM series the gravitational potential well depth and  $\sigma$  vary while  $\Sigma$  and  $\tau$  do not. For the R, M, and RM series, we set  $\kappa = 20 \text{ cm}^2 \text{ g}^{-1}$ . This value is likely larger than realistic values for Solar metallicity. However, we find from the K series that radiation does not have significant effects for lower values of  $\kappa$ , and in the interest of exploring how the dynamical outcomes depend on cloud size and mass we must choose a larger value of  $\kappa$ .

For computational expediency, we use  $\hat{c} = 5(\sigma + c_s)\tau$  in runs K30, K40, R7.1, and M2, instead of the larger value  $\hat{c} = 10(\sigma + c_s)\tau$  used in all other runs. Our studies have shown that the typical values of  $\tau_{90\%}$  are in fact converged with respect to this somewhat relaxed criterion (see Figure 1).

### 3. RESULTS

#### 3.1. Evolution of a Fiducial Model

We begin by describing the overall evolution of a fiducial case. To illustrate key features of the interaction between the turbulent gas of the cloud and the diffuse radiation field that permeates it, we select the model with  $\kappa = 20 \text{ cm}^2 \text{ g}^{-1}$ ,  $R_{\text{cloud}} = 10 \text{ pc}$ , and  $M_{\text{cloud}} = 10^6 M_{\odot}$ . This run has initial properties as listed, e.g., under K20 in Table 1. Figure 2 shows the history of the mass of gas within the box, the mass ejected, and the total mass of all star particles.

Over time, the gas mass steadily declines (slowing after  $2 t_{\text{ff}}$ ), the ejected mass steadily increases, and the mass

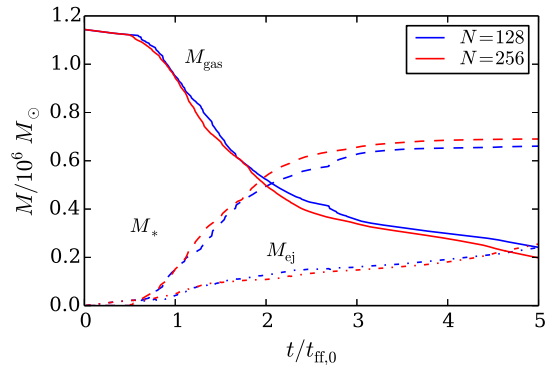


**Figure 3.** Effect of resolution on the mass history of the fiducial model (see K20 in Table 1). After 5 free-fall times, the variation of the final stellar mass is of order 5%, indicating that the evolution of the simulations is acceptably converged at a resolution of  $N = 256$ .

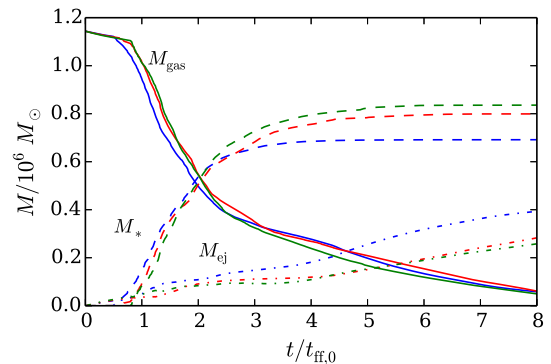


**Figure 4.** Effect of the detailed initial turbulent velocity field on the mass history of the fiducial model (see K20 in Table 1). Red, green, and blue curves represent three distinct realizations of the initial turbulence spectrum (i.e., produced by three differently seeded random number sequences), all with the same initial kinetic energy. After 8 free-fall times, the variation of the final stellar and ejected masses is of order 10%.

in star particles increases rapidly between  $\sim 1 - 2 t_{\text{ff}}$ , and then reaches a plateau. Accretion onto the star particles effectively ceases after  $\sim 3 t_{\text{ff}}$ , because the strong outward radiation force exceeds the inward gravitational force. Over the duration of the simulations,  $\sim 60\%$  of the initial mass in the box (or  $70\%$  of the initial cloud mass) is accreted onto the star particles. Although a small amount of gas ( $\sim 10\%$  of the total) is ejected from the box at early times (because a portion of the turbulent cloud had sufficiently large initial velocities to escape), the gas ejection at  $t \gtrsim 3 t_{\text{ff}}$  is driven by the radiation force.

The standard resolution of our simulations,  $N = 256$ , is dictated by the combined constraints of computational cost steeply increasing with resolution, and the desire to explore a range of parameters. Although the details of turbulence models are always subject to resolution, we have confirmed that the overall evolution of our simulations is acceptably converged. Figure 3 shows the mass histories analogous to Figure 2, comparing results for resolutions  $N = 128$  and  $N = 256$  for the first 5 free-fall times. Evidently, the variations are only of order 5%. We note that different seeds for the random number generator used to form the initial turbulent velocity field (with



**Table 1**  
Initial Model Parameters

Model	$\kappa$ ( $\text{cm}^2 \text{ g}^{-1}$ )	$R_{\text{cloud}}$ (pc)	$M_{\text{cloud}}$ ( $10^6 M_{\odot}$ )	$\Sigma$ ( $\text{g cm}^{-2}$ )	$\sigma$ ( $\text{km s}^{-1}$ )	$f_{\text{Edd},*}$	$\tau^{\text{a}}$	$t_{\text{ff}}$ (Myr)	$\hat{c}$ ( $10^3 \text{ km s}^{-1}$ )
K1	1	10	1	0.67	23	0.068	1	0.54	0.25
K5	5	10	1	0.67	23	0.34	5	0.54	1.2
K10	10	10	1	0.67	23	0.68	10	0.54	2.5
<b>K20</b> <sup>b</sup>	20	10	1	0.67	23	1.4	20	0.54	4.9
K30	30	10	1	0.67	23	2.0	30	0.54	4.9
K40	40	10	1	0.67	23	2.7	40	0.54	4.9
R7.1	20	$10/\sqrt{2}$	1	1.30	27	1.4	40	0.32	5.8
<b>R10</b> <sup>b</sup>	20	10	1	0.67	23	1.4	20	0.54	4.9
R14.1	20	$10\sqrt{2}$	1	0.33	19	1.4	10	0.90	2.1
M0.5	20	10	0.5	0.33	16	1.4	10	0.76	1.8
<b>M1</b> <sup>b</sup>	20	10	1	0.67	23	1.4	20	0.54	4.9
M2	20	10	2	1.30	32	1.4	40	0.38	6.8
R5M0.25	20	5	0.25	0.67	16	1.4	20	0.38	3.6
R7.1M0.5	20	$10/\sqrt{2}$	0.5	0.67	19	1.4	20	0.32	4.2
<b>R10M1</b> <sup>b</sup>	20	10	1	0.67	23	1.4	20	0.54	4.9
R14.1M2	20	$10\sqrt{2}$	2	0.67	27	1.4	20	0.90	5.8
R20M4	20	20	4	0.67	32	1.4	20	0.76	6.8

<sup>a</sup> The optical depth through the center of the initial uniform cloud,  $\tau \equiv 2\kappa R_{\text{cloud}} M_{\text{cloud}} / (\frac{4}{3}\pi R_{\text{cloud}}^3) \equiv \frac{3}{2}\kappa\Sigma$ .

<sup>b</sup> The parameters for these runs (in bold face) are identical and refer to our fiducial model.

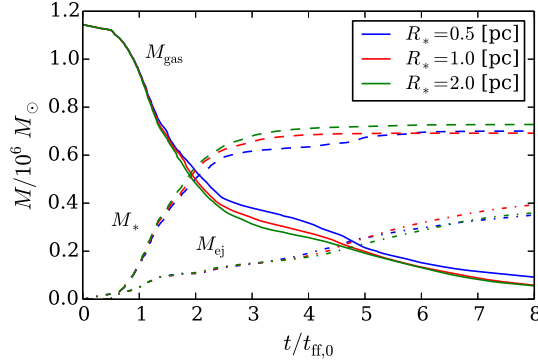


**Figure 5.** Effect of the source size,  $R_*$ , on the mass history of the fiducial model (see K20 in Table 1). After 5 free-fall times, the variation of the final stellar and ejected masses is of order 5% for runs with  $R_*$  a factor of 2 larger and smaller than the fiducial size  $R_* = 1$  pc.

a given total kinetic energy) can also lead to of order 10% variation in the mass history of a cloud, as shown in Figure 4. Finally, we note that the physical size of the source,  $R_*$ , used in Equation 3, leads to of order 5% variation in the mass histories for values a factor of 2 above and below the fiducial source value of  $R_* = 1$  pc, as shown in Figure 5.

The action of the radiation force on the gas can be seen in snapshots of the structure within the cloud at different stages of its evolution, as shown in Figure 6. In all of the snapshots, the gas density is highly clumpy and filamentary due to the turbulence. The radiation energy density is highest immediately surrounding star particles, and has other local variations due to interaction with the gas. Overall, the radiation energy density decreases outward, as does the gas density. The radiation flux points primarily radially away from near the center of box, where the most luminous star particles are found, except in the immediate vicinity of other star particles. Inspection of Figure 6 shows that unlike in implemen-

tations of RHD that adopt flux-limited diffusion (FLD) methods, the radiation flux vectors (unscaled by magnitude) point independently from the gradient in the radiation energy density. Thus, the radiation force is not necessarily co-aligned with the negative gradient of the radiation energy density, as it is by construction in FLD-based implementations. For comparison, Figure 7 shows snapshots of  $\Sigma_z \equiv \int \rho dz$ , the gas surface density in the  $z$ -direction at the same times shown in Figure 6.

Over time, the mean density decreases as gas is expelled from the volume. The gas remains turbulent and filamentary throughout the evolution, and expansion does not lead to the kind of simple shell-like structure that results for non-turbulent clouds (as seen, e.g., for the simple test shown in Fig. 23 and 26 of SO13). Figure 8 shows the mass-weighted RMS gas velocity,  $v_{\text{RMS}} \equiv (2E_{\text{kin}}/M_{\text{gas}})^{1/2}$ , where  $E_{\text{kin}}$  and  $M_{\text{gas}}$  are respectively the total kinetic energy and mass of the gas remaining on the grid, over the evolution of the fiducial model. This velocity declines over  $\sim t_{\text{ff}}$  as the initial turbulence dissipates, rises as radiation feedback becomes important, and then declines slowly for the remainder of the evolution.

As discussed in Section 1, in addition to limiting the star formation efficiency in a given cloud, radiation feedback from clusters can also inject momentum into the surrounding ISM. Figure 9 shows the total ejected kinetic momentum as a function of time for the fiducial model, which is  $\sim 0.47M_{\text{cloud}}\sigma$  by the end of the run. For the purposes of driving turbulence in the ISM and therefore regulating future star formation (Ostriker & Shetty 2011, hereafter OS11), the most important quantity is the ratio of total kinetic momentum ejected to the total mass in stars formed,  $p_*/M_*$ . For the fiducial model,  $p_*/M_* = 17 \text{ km s}^{-1}$ ; the ratio  $p_*/(M_*\sigma)$  is equal to 0.78. This is consistent with the general expectation discussed in OS11 that  $p_*/M_*$  from IR radiation feedback will be of order the velocity dispersion in the central star cluster that forms.

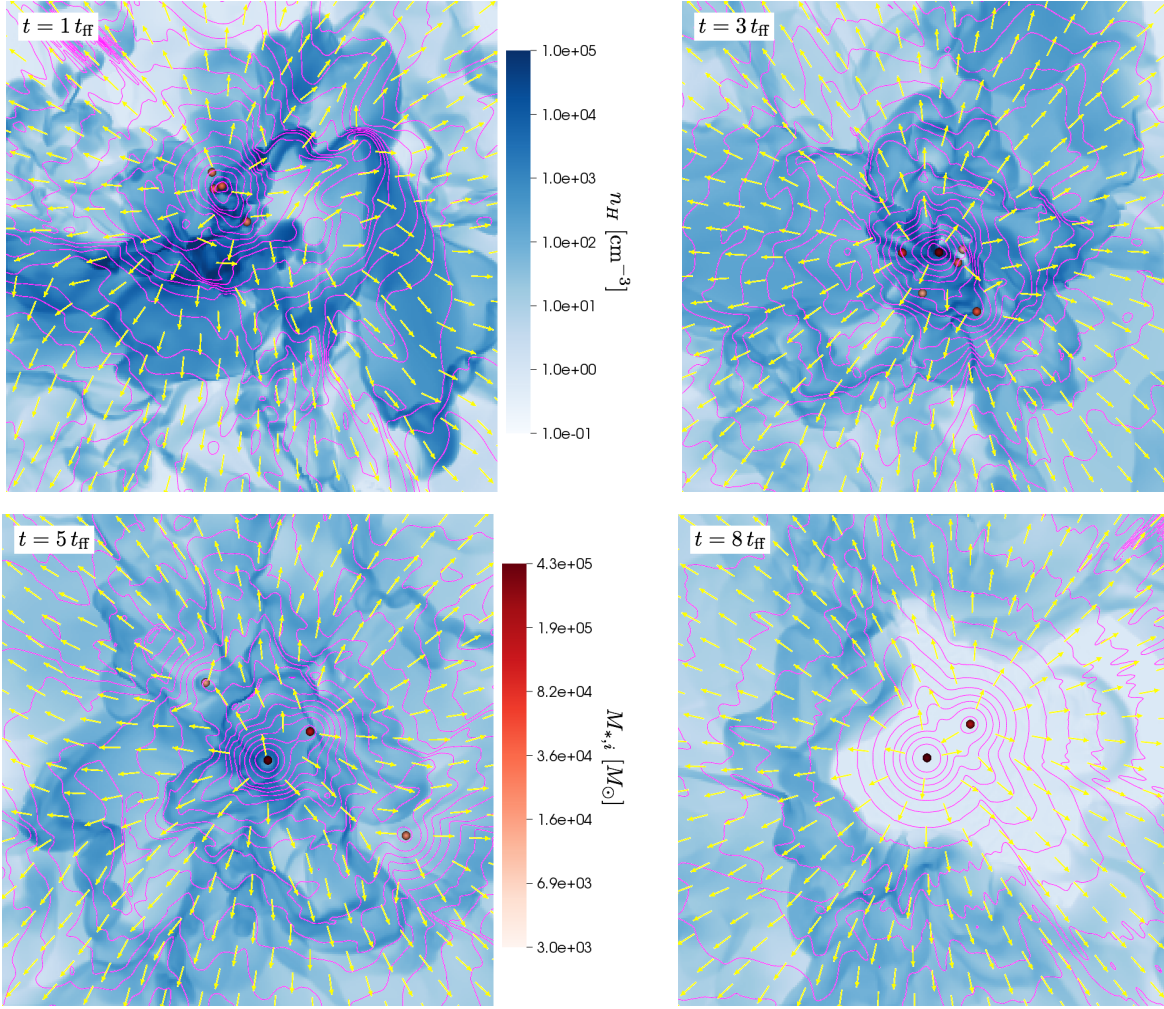


**Figure 6.** Snapshots of slices through the fiducial model, K20, at successive stages in its evolution. Each plot shows the gas number density of hydrogen nuclei  $n_H$  (logarithmic color scale), radiation energy density (contours), direction of radiation flux (vectors), and star particles (spheres with logarithmic color scale indicating mass). The slices are through the most massive star particle in each snapshot, at (top left)  $t = 1 t_{\text{ff}}$  and  $z = 2.8 \text{ pc}$ , (top right)  $t = 3 t_{\text{ff}}$  and  $z = 1.3 \text{ pc}$ , (bottom left)  $t = 5 t_{\text{ff}}$  and  $z = -0.78 \text{ pc}$ , and (bottom right)  $t = 8 t_{\text{ff}}$  and  $z = -2.3 \text{ pc}$ . Star particles within  $\Delta z = \pm 2 \text{ pc}$  of the slice are plotted. The 20 energy density contours are logarithmically spaced over the data range in each slice. The color scale for the gas density (blue, top) is in units of  $\text{cm}^{-3}$ , and the color scale for the star particle mass (red, bottom) is in units of  $M_\odot$ . The slice dimensions are  $40 \times 40 \text{ pc}^2$ .

In Sections 3.3 and 3.4, we discuss further how evolution and outcomes of the simulations vary for different model parameters.

### 3.2. Radiation Structure in a Fiducial Model

In this section, we again employ the fiducial model presented in Section 3.1 and now use it to explore the cloud’s internal radiation structure as well as the competition between radiation and gravity. We wish to investigate the radiative structure after stars have formed and significant feedback is underway, but before the system reaches a limiting state, either by accreting the bulk of the mass onto star clusters or ejecting it from the simulation domain. Thus, we have chosen to take snapshots of the variables at time  $t = 3 t_{\text{ff}}$ .

#### 3.2.1. Radiation and Gravity in a Spherical System

Throughout this section, we compare our results to those of an isotropic dusty gas sphere surrounding a single, centrally-located massive and luminous cluster (cf. Appendix A of OS11) (see also Elmegreen 1983; Scoville

et al. 2001; Krumholz & Matzner 2009; Murray et al. 2010). For this system, in steady state the radiation flux is  $F_{r,*} = L_*/(4\pi r^2) = \Psi M_*/(4\pi r^2)$ , and the gravitational field from the cluster is  $g_* = GM_*/r^2$ . Within any radial shell of mass  $\delta M$ , the ratio of the total radial radiation force  $\kappa F_{r,*} \delta M/c$  to the total radial gravitational force  $g_* \delta M$  from the cluster is therefore

$$f_{\text{Edd},*} \equiv \frac{\kappa F_{r,*}}{c g_*} = \frac{\kappa \Psi}{4\pi c G} \quad (9)$$

$$= 0.68 \left( \frac{\kappa}{10 \text{ cm}^2 \text{ g}^{-1}} \right) \left( \frac{\Psi}{1700 \text{ erg s}^{-1} \text{ g}^{-1}} \right).$$

Including the self-gravity from the gaseous sphere, the ratio of the outward force to the inward force on a radial shell at  $r$  is

$$f_{\text{Edd,sph}}(r) = \frac{f_{\text{Edd},*}}{1 + M_{\text{gas}}(r)/M_*}, \quad (10)$$

where  $M_{\text{gas}}(r)$  is the mass of the gas sphere interior



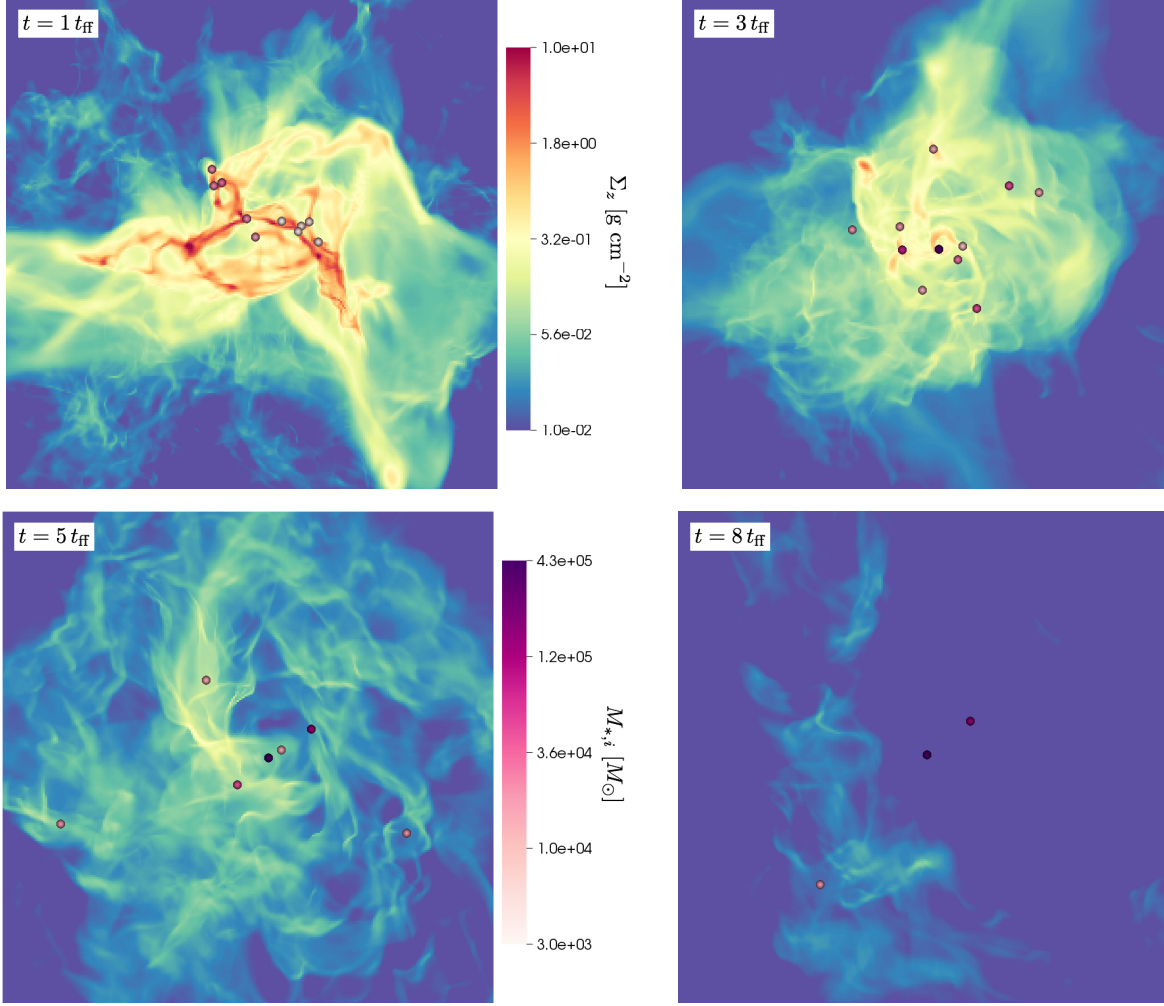


**Figure 7.** Same as Figure 6, but for snapshots of  $\Sigma_z$ , the gas surface density integrated in the  $z$ -direction (logarithmic color scale), along with a two-dimensional projection of all star particles (spheres with logarithmic color scale indicating particle mass  $M_{*,i}$ ). The snapshots are at (top left)  $t = 1 t_{\text{ff}}$ , (top right)  $t = 3 t_{\text{ff}}$ , (bottom left)  $t = 5 t_{\text{ff}}$ , and (bottom right)  $t = 8 t_{\text{ff}}$ . The color scale for the gas surface density (spectrum, top) is in units of  $\text{g cm}^{-2}$ , and the color scale for the star particle mass (violet, bottom) is in units of  $M_{\odot}$ . The image dimensions are  $40 \times 40 \text{ pc}^2$ .

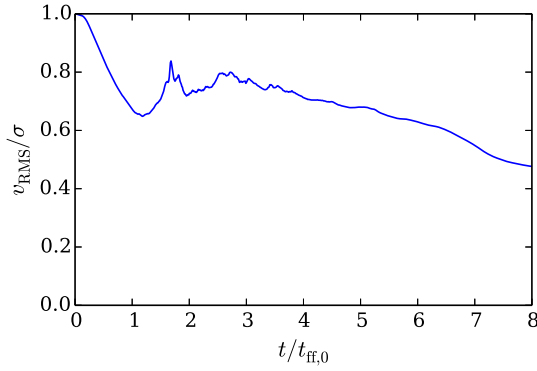


**Figure 8.** Time evolution of the root mean-square (RMS) gas velocity in units of the initial turbulent velocity,  $\sigma$ , for the fiducial model (K20).

to  $r$ . For any gas mass  $M_{\text{gas}}(r)$  less than  $M_{\text{max}} = M_*(f_{\text{Edd},*} - 1)$ , the outward force on a shell at  $r$  exceeds the inward force. For the fiducial model, with  $\kappa = 20 \text{ cm}^2 \text{ g}^{-1}$ ,  $f_{\text{Edd},*} = 1.4$ . As a consequence, if the cloud were able to remain spherically symmetric while

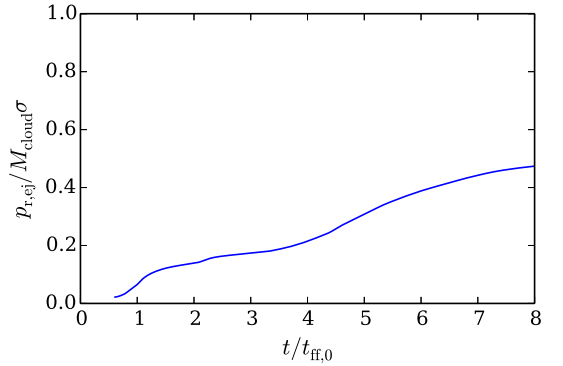


**Figure 9.** Total ejected radial kinetic momentum in the fiducial model (K20). Momentum is measured in units of  $p_{\text{turb,init}} \equiv M_{\text{cloud}} \sigma$ .

forming stars at its center, gas out to a radius for which  $M_{\text{gas}}(r)/M_* = 0.4$  would have the local radiation force exceeding gravity.

If the net efficiency of star formation compared to the initial cloud mass is  $\varepsilon_* = M_*/M_{\text{cloud}}$ , then the total re-

maining gas has  $M_{\text{gas}}(r_{\text{max}})/M_* = (1 - \varepsilon_*)/\varepsilon_*$ . Substitution in Equation (10) shows that the local Eddington ratio  $f_{\text{Edd,sph}}(r)$  would exceed unity at all radii in a spherical cloud when a fraction

$$\varepsilon_{*,\text{sph}} \equiv f_{\text{Edd},*}^{-1} \quad (11)$$

$$= 1.5 \left( \frac{\kappa}{10 \text{ cm}^2 \text{ g}^{-1}} \right)^{-1} \left( \frac{\Psi}{1700 \text{ erg s}^{-1} \text{ g}^{-1}} \right)^{-1}.$$

of the original cloud has been converted to stars.<sup>6</sup> For an idealized spherical system with  $\kappa = 20 \text{ cm}^2 \text{ g}^{-1}$ , 74% of the original cloud would have to be converted to stars for the remainder to be forced outward by radiation. Of course, gas pressure forces can become important, so that gas originally at small radii where  $f_{\text{Edd,sph}}(r) \gg 1$  can sweep up and expel fluid elements that were originally at large radii; this reduces the actual SFE  $\varepsilon_{*,\text{final}}$  below  $\varepsilon_{*,\text{sph}}$ .

The above discussion suggests that unless  $\kappa$  is relatively large, radiation forces will not be able to expel a substantial portion of a cloud's mass. In fact, larger values of  $\kappa$  than would be realistic for IR radiation at Milky Way dust abundances may be required for any gas expulsion, even in the limit of highly efficient star formation. For the idealized spherical case, the (stellar-plus-gas) gravitational force exceeds the radiation force at the outer edge of the cloud even for  $\varepsilon_* \rightarrow 1$  if  $f_{\text{Edd},*} < 1$ . Moreover, for gas very near any star cluster, the dominant forces are radiation and gravity, so only if  $f_{\text{Edd},*} > 1$  can continued accretion be halted. The condition  $f_{\text{Edd},*} > 1$  translates to  $\kappa > \kappa_{\text{crit}}$  where

$$\kappa_{\text{crit}} \equiv \frac{4\pi c G}{\Psi} \quad (12)$$

$$= 15 \text{ cm}^2 \text{ g}^{-1} \left( \frac{\Psi}{1700 \text{ erg s}^{-1} \text{ g}^{-1}} \right)^{-1}.$$

Although the true structure is non-spherical, this explains why we have selected the  $\kappa = 20 \text{ cm}^2 \text{ g}^{-1}$  model for detailed presentation of internal radiation structure: for lower- $\kappa$  models, radiation forces are not expected to be strong enough to prevent continuing accretion and expel substantial amounts of mass.

As we shall next discuss, the simple spherical analysis provides useful guidance regarding the relative importance of radiation and gravity, but the solution of the full RHD equations for a turbulent medium is more complex. In particular, neither the radiation field nor the gravitational field is spherically symmetric, and the gas density on which these fields act is highly nonuniform. The radiation and gravitational forces—locally, averaged over spherical shells, or integrated over the whole cloud—therefore can differ substantially from estimates based on simple spherical models.

### 3.2.2. Analysis of Radiation and Gravity in the Turbulent Cloud

<sup>6</sup> If all the remaining gas is collected in a single thin shell, as for the idealized system described in Appendix A of OS11, self-gravity is diluted so that the ratio of radiation to total gravitational forces is  $f_{\text{Edd}} = f_{\text{Edd},*}/(1 + 0.5M_{\text{shell}}/M_*)$ . Shell expulsion would commence when a fraction  $\varepsilon_{*,\text{sh}} = (2f_{\text{Edd},*} - 1)^{-1}$  of the gas is converted to stars; for the case  $\kappa = 20 \text{ cm}^2 \text{ g}^{-1}$  this would correspond to 56%.

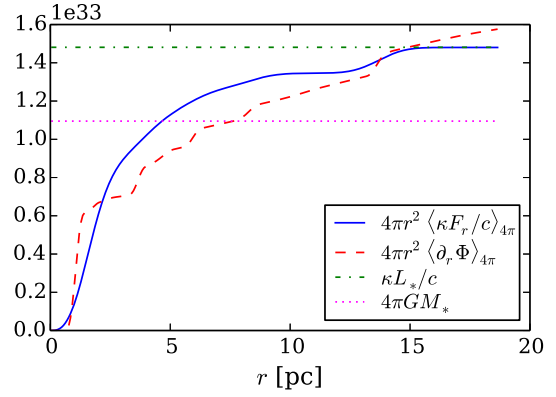


**Figure 10.** Angle-averaged radial radiation force per unit mass,  $\langle \kappa F_r / c \rangle$  (solid), and the angle-averaged total gravitational force per unit mass,  $\langle \partial_r \Phi \rangle$  (dash-dotted), both compensated by  $4\pi r^2$ , for the fiducial run (model K20) at time  $t = 3 t_{\text{ff}}$ . For comparison, we plot  $\kappa L_*/c$  (dashed) and  $4\pi G M_*$  (dotted), the radiation and gravitational forces that would be produced by a point-source cluster with the same total stellar mass as is present at  $t = 3 t_{\text{ff}}$  in the simulation. The measured radiation force reaches 90% of the point-source value at  $\sim 10$  pc from the center of mass, comparable to the radius of the original cloud. At  $r > 15$  pc,  $4\pi r^2 \langle F_r \rangle$  asymptotes to  $L_*$ . The measured gravitational force exceeds the stellar point-source value at large radii because a significant portion of the cloud's gas has neither been accreted nor expelled at this time.

To quantify the internal cloud structure in a simple way, we compute angle-averaged radial profiles, denoted by  $\langle \cdot \rangle_{4\pi}$ . To do this, we first compute the center of mass of the stars,  $\mathbf{r}_{\text{CM}}$ , then linearly interpolate the Cartesian grid data onto an  $N_r \times N_\phi \times N_\theta$  spherical grid with  $N_r = N_\theta = N$  and  $N_\phi = 2N$  zones centered at  $\mathbf{r}_{\text{CM}}$ , with  $r \in [0, 2R_{\text{cloud}} - r_{\text{CM}}]$ .<sup>7</sup> Finally, we average the interpolated data on this grid over all solid angles to obtain a radial profile.

Figure 10 compares, for  $t = 3 t_{\text{ff}}$ , the profiles of the two dominant competing effects in the problem: the outward radial radiation force and the inward gravitational force. These two forces both scale with the mass (or, per unit volume, the density), which we omit here, and both fall off as inverse square laws away from the center of mass of the system; thus, we compensate by a factor of  $4\pi r^2$  in each profile. For comparison, we also plot the radiation and stellar gravity forces/mass that would apply in the limit of a single point mass cluster at  $\mathbf{r}_{\text{CM}}$ , which appear here as constants ( $\kappa L_*/c$  and  $4\pi G M_*$ , respectively) in our radially-compensated plot. Far from the center of mass of the system, the profile of the radiation force approaches that of a point source, reaching 90% of this value by  $r \sim 10$  pc, a distance comparable to the original cloud radius. However, the gravitational force at this time still contains a significant contribution from the remaining gas in the system (at this time, the total mass in gas is  $3.4 \times 10^5 M_\odot$ , while the mass in stars is  $6.6 \times 10^5 M_\odot$ ), so it is slightly higher than the point-source cluster limit at large distance. The mean specific radiation force exceeds the mean specific gravitational force for most of the profile, indicating that in most zones the gas feels a net outward force at this point. Figure 2 shows that the accretion rate onto the sink particles slows between  $t \sim 2 - 3 t_{\text{ff}}$  and essentially stops

<sup>7</sup> Note that  $r_{\text{CM}} \ll 2R_{\text{cloud}}$  typically, so that  $2R_{\text{cloud}} - r_{\text{CM}} \approx L_{\text{box}}/2$ .

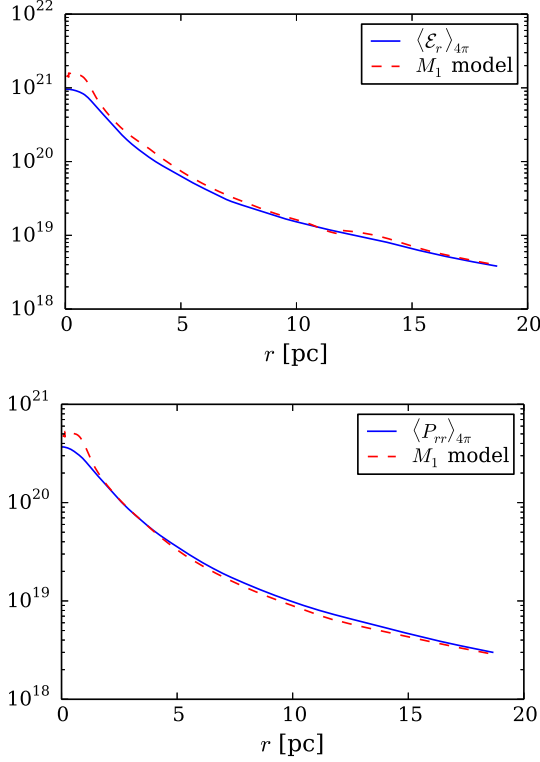


**Figure 11.** Angle-averaged profiles of  $\mathcal{E}$  (top) and  $P_{rr}$  (bottom) for model K20 at time  $t = 3 t_{\text{ff}}$  (solid curves). For comparison, we also plot the semi-analytic solutions (dashed) derived from the  $M_1$  closure for a spherically symmetric system with density and radiation flux profiles given by angle-averages of the simulation data at this time. The measured data and semi-analytic solutions are comparable, showing that the radiation is in a quasi-steady state at this time.

after  $t \sim 3 t_{\text{ff}}$ . We note that in the simple spherical model described above, Equation 12 suggests that radiation forces would exceed gravity forces everywhere only when  $\varepsilon_* \rightarrow 0.7$  for  $\kappa = 20 \text{ cm}^2 \text{ g}^{-1}$ . In fact,  $\varepsilon_*$  is only  $\sim 0.57$  at  $t \sim 3 t_{\text{ff}}$ , somewhat lower than this value.

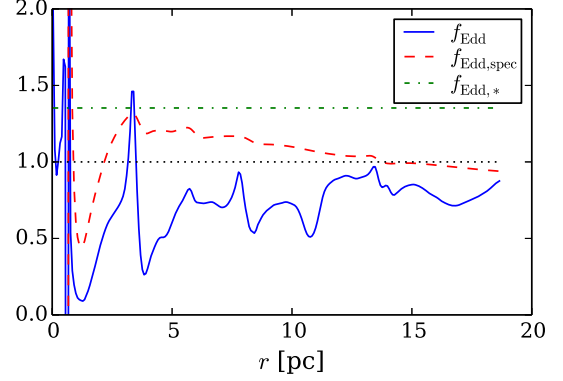
In Figure 11, we plot the radiation energy density,  $\langle \mathcal{E} \rangle_{4\pi}$ , and the radial component of the radiation pressure tensor,  $\langle P_{rr} \rangle_{4\pi}$ , at time  $t = 3 t_{\text{ff}}$ . For comparison, we also plot the semi-analytic solutions for  $\mathcal{E}$  and  $P_{rr}$ , respectively, derived from the  $M_1$  closure for a spherically symmetric system in steady state (see Equations 110 and 111 of SO13). This requires the solution of an ordinary differential equation (ODE)<sup>8</sup> for the reduced flux,  $f \equiv F/(c\mathcal{E})$ , as a function of the radial profiles  $\langle \rho \rangle_{4\pi}$  and  $\langle F_r \rangle_{4\pi}$ . The angle-averaged profiles and semi-analytic models are comparable for both  $\mathcal{E}$  and  $P_{rr}$ , indicating that the radiation field is, in an averaged sense, close to quasi-steady state for the density distribution at this time.

Figure 12 shows (again for model K20 at  $t = 3 t_{\text{ff}}$ ) the radial profile of the Eddington factor, defined by

$$f_{\text{Edd}}(r) \equiv \frac{\langle \rho \kappa F_r / c \rangle_{4\pi}}{\langle \rho \partial_r \Phi \rangle_{4\pi}}, \quad (13)$$

where the angular averages in Equation (13) are over local spherical shells. The quantity  $f_{\text{Edd}}(r)$  measures the

<sup>8</sup> This ODE has a regular singularity at  $f = 2\sqrt{3}/5 \sim 0.7$  that poses numerical difficulties in its solution, resulting in a slight shift in the comparison profile near  $\sim 12$  pc for model K20 in Figure 11.



**Figure 12.** Radial profile of the Eddington factor,  $f_{\text{Edd}}$  (solid), averaged over local spherical shells (see Equation 13) for model K20 at  $t = 3 t_{\text{ff}}$ . The local Eddington ratio is less than 1 (dotted) over most of the domain, indicating that the majority of the gas in the cloud feels a net inward force. The ratio of angle-averaged *specific* forces,  $f_{\text{Edd,spec}} \equiv \langle \kappa F_r / c \rangle_{4\pi} / \langle \partial_r \Phi \rangle_{4\pi}$  is also shown (dash-dotted) for comparison; this exceeds unity for most radii. The dashed line shows  $f_{\text{Edd,*}}$  (see Equation 10), the Eddington ratio for a simple spherical model with negligible gas self-gravity.

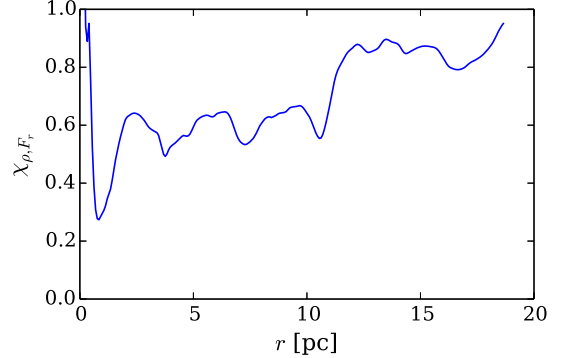


**Figure 13.** Radial profile of  $\chi_{\rho,F_r}$ , the correlation fraction between  $\rho$  and  $F_r$  (see Equation 14) for model K20 at  $t = 3 t_{\text{ff}}$ . Values of  $\chi_{\rho,F_r}$  less than unity show that  $\rho$  and  $F_r$  are somewhat anti-correlated over most of the domain.

ratio of the total radial radiation force acting on the gas to the total gravitational force acting on that gas, within a shell at a given radius. For comparison, we show the ratio of angle-averaged *specific* forces  $f_{\text{Edd,spec}}(r)$ ; i.e., with the density omitted from Equation (13). As previously seen in Figure 10, where the angle-averaged specific radiation force exceeds that of gravity at most radii,  $f_{\text{Edd,spec}}(r) > 1$  almost everywhere. In contrast, the ratio of angle-averaged total forces  $f_{\text{Edd}}(r)$  is below 1 for most of the profile. For reference, we also show the quantity  $f_{\text{Edd,*}}$  defined in Equation (10); this is well above both  $f_{\text{Edd,spec}}(r)$  and  $f_{\text{Edd}}(r)$  because self-gravity adds appreciably to the gravity of the stars at this time. The difference between  $f_{\text{Edd}}$  and  $f_{\text{Edd,spec}}$  suggests that the radiation flux and gas density must be anti-correlated to some extent, and highlights the importance of conducting fully three-dimensional simulations.

In Figure 13, we plot the profile of  $\chi_{\rho,F_r}$ , the correlation fraction of  $\rho$  and  $F_r$ , defined as

$$\chi_{\rho,F_r} \equiv \frac{\langle \rho F_r \rangle_{4\pi}}{\langle \rho \rangle_{4\pi} \langle F_r \rangle_{4\pi}}. \quad (14)$$

When  $\chi_{\rho,F_r} = 1$ , the gas density and radiation flux in a

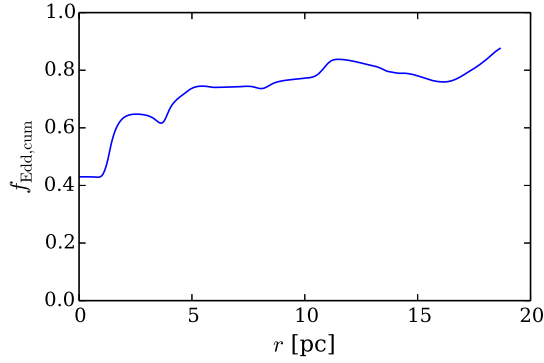


**Figure 14.** Radial profile of the cumulative Eddington ratio,  $f_{\text{Edd,cum}}(r)$  (see Equation 15), measured inward from the largest radius in the interpolation grid for model K20 at  $t = 3 t_{\text{ff}}$ . Since  $f_{\text{Edd,cum}}(r) < 1$  over the entire domain, the gas feels a net inward force.

given radial shell have uncorrelated fluctuations, whereas  $\chi_{\rho, F_r} < 1$  implies that the fluctuations about the mean are anti-correlated. Figure 13 indicates that there is some degree of anti-correlation between  $\rho$  and  $F_r$ , which explains why  $f_{\text{Edd}}$  lies below  $f_{\text{Edd,spec}}$ .

Figure 14 shows the radial profile of  $f_{\text{Edd,cum}}$ , the cumulative integral of  $f_{\text{Edd}}$  defined as

$$f_{\text{Edd,cum}}(r) \equiv \frac{\int_r^{r_{\text{max}}} \langle \rho \kappa F_r / c \rangle_{4\pi} 4\pi r^2 dr}{\int_r^{r_{\text{max}}} \langle \rho \partial_r \Phi \rangle_{4\pi} 4\pi r^2 dr}. \quad (15)$$

Note that in Equation (15), the volume integrals are cumulative, starting from the maximum radius of the spherical interpolation grid, instead of only over local shells as in Equation (13). Once again, this shows that the net force that the majority of the gas feels is inward, since  $f_{\text{Edd,cum}} < 1$  throughout the domain. We note, however, that in spite of the *net* inward force, and the *overall* anti-correlation in the fluctuations of density and radiation flux, individual fluid elements can experience a radiation force (potentially aided by a pressure force) that exceeds the gravitational force. This is why, as shown in Figures 2 and 9, mass and momentum can be ejected by the action of radiation forces.

In analytic models, effects of reprocessed IR radiation are sometimes described in terms of a radiation “trapping factor” (e.g., Krumholz & Matzner 2009). This measures the enhancement in the radiation force due to reprocessed radiation energy trapped in an opaque cloud. The trapping factor is defined as a ratio of the radial radiation force on the gas to the force  $L_*/c$  that would apply in the single-absorption limit.<sup>9</sup> In Figure 15, we plot the cumulative profile of the trapping factor defined by

$$f_{\text{trap,cum}}(r) \equiv \frac{\int_r^{r_{\text{max}}} \langle \rho \kappa F_r / c \rangle_{4\pi} 4\pi r^2 dr}{L_*/c}, \quad (16)$$

in comparison to the cumulative optical depth  $\tau(r)$  defined by

$$\tau(r) \equiv \int_r^{r_{\text{max}}} \langle \rho \kappa \rangle_{4\pi} dr. \quad (17)$$

Both quantities are measured radially-inward from the

<sup>9</sup> Note that we do not include UV radiation in these simulations, so the trapping factor here only includes effects of IR radiation.

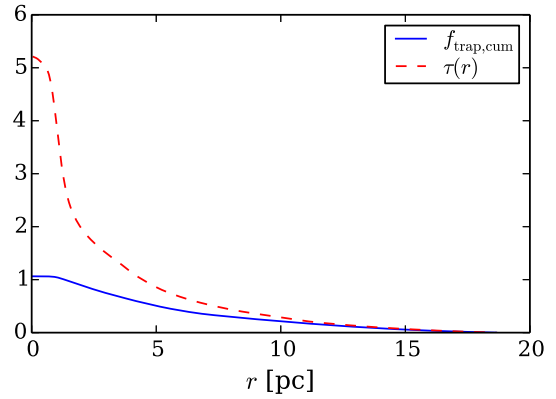


**Figure 15.** Radial profile of the cumulative trapping factor,  $f_{\text{trap,cum}}(r)$  (see Equation 16), measured inward from the largest radius in the interpolation grid (solid), for model K20 at  $t = 3 t_{\text{ff}}$ . Also shown (dashed) is the optical depth  $\tau(r)$  (see Equation 17), also measured radially-inward. For a simple spherical system with a central point source, these would be identical; the discrepancy here is explained by the anti-correlation of  $\rho$  and  $F_r$  and the distribution of star formation.

maximum radius of the interpolation grid. For a spherical, isotropic radiation field of a point source and a spherical gas density profile,  $f_{\text{trap,cum}}(r)$  and  $\tau(r)$  would be identical. However, Figure 15 shows that  $f_{\text{trap,cum}}(r)$  is substantially less than  $\tau(r)$  (and is less than 1 over most of the domain). Once again, much of this difference is explained by the anti-correlation between  $\rho$  and  $F_r$ , as demonstrated in Figure 13. In addition, the fact that sources are distributed rather than concentrated in a single central point implies that the flux is not radially directed at small  $r$ ; the high density in this region therefore leads to a greater contribution to  $\tau$  (Equation 17) than to  $f_{\text{trap,cum}}$  (Equation 16). We note that for the present models, the source distribution is in part due to the spatial separation of multiple sink particles, and in part due to the finite size of each radiation source ( $\sim R_* = 1$  pc; see Equation 3).

### 3.3. Effects of Varying Opacity

Here we present the results from the K series, in which we vary the opacity while holding the cloud mass and radius fixed (see Table 1 for input parameter values). As explained in Section 2.2, we use a wide range of  $\kappa$ ; this range contains values that substantially exceed the realistic mean opacity of dust to IR in star-forming GMCs for Solar neighborhood dust abundance, but it allows us to study the physical dependence of the cloud outcomes on this principal parameter. In particular, the discussion leading to Equation 13 suggests that the potential for reprocessed radiation to drive substantial mass loss from a cloud depends primarily on  $\kappa$ . In high dust abundance systems (either galaxies/ISM regions with high metallicity, or locally dust-enriched individual clouds),  $\kappa$  may be in the regime where reprocessed radiation forces become quite important.

The comparative properties for Series K are summarized in Table 2, where  $\varepsilon_* \equiv M_*/M_{\text{tot}}$  and  $\varepsilon_{\text{gas}} \equiv M_{\text{gas}}/M_{\text{tot}}$  are measured over the entire computational domain, with the total mass defined as  $M_{\text{tot}} \equiv M_* + M_{\text{gas}} + M_{\text{ej}}$ ;  $f_{\text{Edd,cum}}(r)$ ,  $f_{\text{trap,cum}}(r)$ , and  $\tau(r)$  are measured over the entire spherical interpolation domain for  $r \rightarrow 0$  (see Equations 15, 16, 17); and  $\langle \chi_{\rho, F_r} \rangle_r$  is averaged



over the spherical interpolation domain. The quantity  $\varepsilon_{\text{ej}} \equiv M_{\text{ej}}/M_{\text{tot}}$  is measured from the time integral of the mass flux through the surfaces of the computational box. We report results from analysis at time  $t = 3 t_{\text{ff}}$ , which is after significant star formation feedback has begun, but before that feedback can destroy the cloud.

As expected (cf. Equation 12), the star formation efficiency  $\varepsilon_*$  decreases as  $\kappa$  increases. Correspondingly, both the fraction of gas remaining in the computational domain,  $\varepsilon_{\text{gas}}$ , and the fraction ejected,<sup>10</sup>  $\varepsilon_{\text{ej}}$ , increase somewhat with increasing opacity. However, the differences in these intermediate efficiencies at  $t = 3 t_{\text{ff}}$  are less than at late times, because the dynamical effect from radiation requires more time to develop fully.

In addition to the differences of the efficiencies with  $\kappa$ , Table 2 shows a number of other interesting effects. First, the Eddington ratio integrated over the whole (spherical) domain,  $f_{\text{Edd,cum}}(r \rightarrow 0)$ , increases with  $\kappa$ . However, in all cases it remains less than unity. Moreover, the correlation between gas and radiation flux,  $\langle \chi_{\rho, F_r} \rangle_r$ , decreases as  $\kappa$  increases for the models with  $f_{\text{Edd},*} > 1$ . That is, cases with increasing potential for radiation to overwhelm gravity (larger  $f_{\text{Edd},*}$ ) in part compensate for this with an increasing anti-correlation of gas and radiation. We further find that the cumulative trapping factor,  $f_{\text{trap,cum}}(r \rightarrow 0)$ , can be far smaller than the integrated optical depth  $\tau(r \rightarrow 0)$  from the center to the edge of the cloud; the ratio is a factor of 4 or 5 for the  $f_{\text{Edd},*} > 1$  models. Thus, the estimate  $\tau L/c$ , sometimes used in subgrid models (within galaxy formation simulations) to represent the force from reprocessed radiation, can substantially overestimate the true radiation force.

Figures 16 - 18 show the time evolution out to  $t = 8 t_{\text{ff}}$  of several diagnostic variables. Figure 16 shows the time evolution of the mass fractions,  $\varepsilon_*$ ,  $\varepsilon_{\text{gas}}$ , and  $\varepsilon_{\text{ej}}$ . On the one hand, the time evolution of  $\varepsilon_{\text{gas}}$  is similar for all values of  $\kappa$ , with variations of up to 5-10% over all runs in the K series. By time  $t = 8 t_{\text{ff}}$ , less than 10% of the original mass of the cloud remains, with almost all of the gas in each run either accreted onto star particles or expelled from the domain. On the other hand, the evolutions of  $\varepsilon_*$  and  $\varepsilon_{\text{ej}}$  depend strongly on  $\kappa$ ; as  $\kappa$  increases,  $\varepsilon_*$  decreases and  $\varepsilon_{\text{ej}}$  increases. Figure 16 shows a clear break between models in the group with  $\kappa = 1, 5, 10$ , compared to the group  $\kappa = 20, 30, 40$ . These groups have  $f_{\text{Edd},*} < 1$  and  $f_{\text{Edd},*} > 1$ , respectively, so the break is consistent with general expectations discussed in Section 3.2.1

There are additional more subtle effects as well. First, note that runs K1 and K5 have almost identical mass ejection. This is essentially the same as the mass that would be ejected in the absence of radiation, due to a small fraction ( $\sim 10\%$ ) of the initial mass in the cloud being unbound. For  $\kappa = 10$ , the effects of radiation begins to be seen in reducing  $\varepsilon_*$  and increasing  $\varepsilon_{\text{ej}}$  (starting at  $\sim 3 t_{\text{ff}}$ ). For the large- $\kappa$  group, the final value of  $\varepsilon_*$  is reached by  $t = 4 t_{\text{ff}}$  in all cases. However, gas ejection occurs more rapidly in run K40 than in the K20 and K10 runs. For large  $\kappa$ , the final values of both  $\varepsilon_*$  and  $\varepsilon_{\text{ej}}$

<sup>10</sup> It is not sufficient merely to note that the gas has left the computational domain through the outer boundary to conclude that it has been driven out as a wind, especially considering the “diode” outflow boundary condition we employ prevents gas from (re)entering through the same boundary. In principle, some of the ejected gas might be able to return.

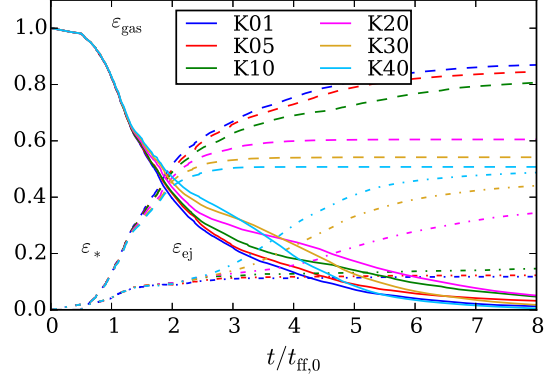


**Figure 16.** Time evolution of the mass fractions,  $\varepsilon_* \equiv M_*/M_{\text{tot}}$  (dashed),  $\varepsilon_{\text{gas}} \equiv M_{\text{gas}}/M_{\text{tot}}$  (solid), and  $\varepsilon_{\text{ej}} \equiv M_{\text{ej}}/M_{\text{tot}}$  (dash-dotted), where  $M_{\text{tot}} \equiv M_* + M_{\text{gas}} + M_{\text{ej}}$  for the runs in the K series. Low- $\kappa$  models K01, K05, and K10 have  $f_{\text{Edd},*} < 1$ , while high- $\kappa$  models K20, K30, K40 have  $f_{\text{Edd},*} > 1$ . There is a clear break in  $\varepsilon_*$  and  $\varepsilon_{\text{ej}}$  between these groups. Time is in units of the initial free-fall time,  $t_{\text{ff}}$ , for each model.

approach 0.5.

Figure 17 shows the time evolution of  $p_{r,\text{ej}}/(M_{\text{cloud}}\sigma)$ , the time-integrated radial kinetic momentum ejected from the grid (in the center of mass frame of the GMC), in units of the characteristic initial turbulent momentum of the cloud  $p_{\text{turb,init}} \equiv M_{\text{cloud}}\sigma$ . Similar to the results for the ejected mass, there is a clear break between the low- and high- $\kappa$  models. In all runs,  $p_{r,\text{ej}}$  increases similarly up to  $\sim 2 t_{\text{ff}}$ , due to the initial turbulence expelling some of the gas from the grid. After  $t = 2 t_{\text{ff}}$ , the additional kinetic momentum ejected over the course of the simulation is negligible for runs K1, K5, and K10, where  $f_{\text{Edd},*} < 1$ , and increases dramatically with  $\kappa$  for runs K20, K30, and K40, where  $f_{\text{Edd},*} > 1$ .

Finally, Figure 18 shows the time evolution of  $\alpha_{\text{vir}} \equiv 2E_{\text{kin,gas}}/E_{\text{grav,gas}}$ , the total virial parameter for the gas on the grid. The simulations begin with  $\alpha_{\text{vir}} = 2$ , i.e., with the cloud in the just-bound state. Then, after a decrease up to  $t \sim t_{\text{ff}}$  due to the decay of the initial turbulence, the virial parameter increases again once star formation begins. For runs K1, K5, and K10,  $\alpha_{\text{vir}}$  settles into a roughly steady value between 1 and 1.5, i.e., close to virial equilibrium. In contrast, for runs K20, K30, and K40, the virial parameters rapidly diverge, with larger- $\kappa$  models diverging earlier, as the cloud is disrupted by radiation from the newly formed stars and the unaccreted gas is ejected from the grid. Similar to the results shown in Figure 17, this suggests that a state change occurs in systems with  $f_{\text{Edd},*} \gtrsim 1$  so that the gas quickly becomes unbound and is dispersed back into the diffuse ISM.

#### 3.4. Cloud Evolution Outcomes: Parameter Study

In this section, we examine the final outcomes for each series in our parameter study. Table 3 summarizes the results from each series described in Section 2.2 with model parameters given in Table 1. From these data, several general trends are evident. First, we examine trends in the final outcomes of the K series, in which the opacity  $\kappa$  is varied independently of the other simulation parameters. As discussed in Section 3.3, the star formation efficiency  $\varepsilon_{*,\text{final}}$  decreases with increasing opacity, with a clear division between models K10 and K20 near the critical value of  $f_{\text{Edd},*} = 1$ . This division is also clearly



**Table 2**  
Intermediate Outcomes from Varying the Opacity

Model	$f_{\text{Edd},*}$	$\varepsilon_*$	$\varepsilon_{\text{gas}}$	$\varepsilon_{\text{ej}}$	$f_{\text{Edd,cum}}^a$	$\langle \chi_{\rho, F_r} \rangle_r^b$	$f_{\text{trap,cum}}^a$	$\tau^a$
K01	0.068	0.67	0.22	0.11	0.032	0.82	0.074	0.24
K05	0.34	0.66	0.23	0.11	0.12	0.77	0.25	1.1
K10	0.68	0.63	0.25	0.12	0.17	0.79	0.55	3.0
<b>K20</b>	1.4	0.57	0.30	0.13	0.43	0.81	1.1	5.2
K30	2.0	0.53	0.33	0.14	0.60	0.70	1.2	4.9
K40	2.7	0.50	0.33	0.16	0.99	0.63	1.1	4.1

**Note.** — Intermediate outcomes for the K series, in which the opacity is varied. All results are given at time  $t = 3 t_{\text{ff}}$ .

<sup>a</sup> Measured over the spherical interpolation grid, for  $r \rightarrow 0$ .

<sup>b</sup> Measured over spherical shells, then radially averaged.

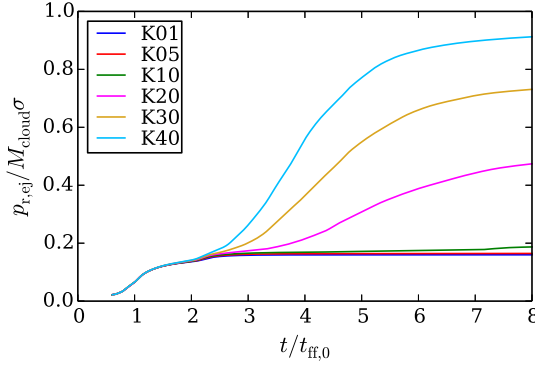


**Figure 17.** Time evolution of  $p_{r,\text{ej}}/p_{\text{turb,init}}$ , the time-integrated radial component of the kinetic momentum ejected from the grid, in the center of mass frame of the star particles, in units of the initial turbulent momentum  $p_{\text{turb,init}} \equiv M_{\text{cloud}}\sigma$ , for the runs in the K series. Only models with  $f_{\text{Edd},*} > 1$  (K20, K30, K40) have substantial momentum loss driven by radiation.

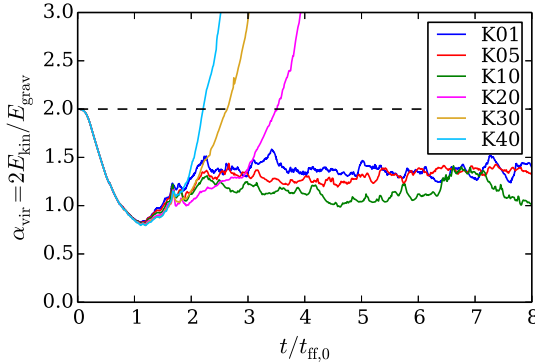


**Figure 18.** Time evolution of  $\alpha_{\text{vir}} = 2E_{\text{kin}}/E_{\text{grav}}$ , the total virial parameter for the gas on the grid, for the runs in the K series. Note that the clouds with  $\kappa > \kappa_{\text{crit}}$  rapidly become unbound, within a few free-fall times, and do so sooner with increasing  $\kappa$ .

seen in the values of  $p_{r,\text{ej}}$ , the total radial kinetic momentum ejected from the simulation grid. Table 3 includes results for  $p_{r,\text{ej}}$  normalized in three different ways, and for all choices the values from  $\kappa \leq 10$  models are all similar, while the values are much larger for  $\kappa \geq 20$ .

Second, we examine the simulation outcomes in the R, M, and RM series as a function of the cloud surface density and Mach number. The opacity is  $\kappa = 20$  for all of these models, so that  $f_{\text{Edd},*} = 1.4$ . On the one hand, the star formation efficiencies are all comparable throughout the RM series, where the surface density and

opacity are held constant as the cloud radius and mass are varied. On the other hand, as the cloud radius and mass are independently varied in the R and M series, respectively, the cloud surface density changes, and there is a much stronger variation in the star formation efficiencies in these series. This suggests that—all else being equal—clouds with higher surface density eject a smaller fraction of their initial mass. Interestingly, the trend for  $\varepsilon_{*,\text{final}}$  with  $\tau$  is the opposite in varying- $\Sigma$  models from varying- $\kappa$  models. That is, an increase of  $\kappa$  for fixed cloud mass and radius decreases  $\varepsilon_{*,\text{final}}$ , whereas an increase of mass or decrease of radius for fixed  $\kappa$  increases  $\varepsilon_{*,\text{final}}$ . Also, we note that the pairs (M0.5,M1) and (R5M0.25, R10M1) have the same matched values of the initial velocity dispersion (16 and 23  $\text{km s}^{-1}$ , see Table 1), but  $\varepsilon_{*,\text{final}}$  varies more strongly for the M series than for the RM series. That is, surface density appears to be more important than the potential well depth for the final star formation efficiency of a cloud.

We further note that although  $f_{\text{Edd},*} > 1$  distinguishes models in which  $\varepsilon_*$  is reduced by radiation from those in which radiation does not affect  $\varepsilon_*$ , the values  $\varepsilon_{*,\text{final}}$  in Table 3 are *not* consistent with Equation (12). In particular, the R, M, and RM series all have  $f_{\text{Edd},*} = 1.4$  and  $\varepsilon_{*,\text{sph}} = 0.74$ , while Table 3 shows a range of values for  $\varepsilon_{*,\text{final}}$ . Similarly,  $\varepsilon_{*,\text{sph}}$  decreases from 0.74 to 0.37 from K20 to K40, but the decrease in  $\varepsilon_{*,\text{final}}$  is fractionally smaller. This shows that a simple “Eddington-type” spherical model is inadequate for quantitatively predicting the net SFE in a cloud, as controlled by radiation feedback.

In all series, we see that  $p_{r,\text{ej}}/M_*$ , the kinetic momentum ejected per stellar mass formed, is comparable to the initial velocity dispersion  $\sigma$  of the clouds, to within a factor of 2 for all runs with  $f_{\text{Edd},*} > 1$ . The values are between 10 and 40  $\text{km s}^{-1}$ . Interestingly, just as for  $\varepsilon_{*,\text{final}}$ , the ratio  $p_{r,\text{ej}}/M_*$  appears to depend more strongly on the cloud’s surface density than its potential well depth; all the models in the RM series have essentially the same value of  $p_{r,\text{ej}}/M_*$  even though they have varying potential well depth (i.e., varying  $\sigma$ ), while  $p_{r,\text{ej}}/M_*$  increases toward higher  $\Sigma$  models in the R and M series.

In principle, it is possible that some fraction of the gas that is ejected from the simulation grid might in reality ultimately be able to re-collapse. As a proxy for whether or not the gas can re-collapse, we compute the escape velocity

$$v_{\text{esc}} \equiv \left( \frac{2GM_{\text{cloud}}}{R_{\text{box}}} \right)^{1/2}, \quad (18)$$

**Table 3**  
Final Outcomes

Model	$\varepsilon_{*,\text{sph}}$	$\varepsilon_{*,\text{final}}$	$\varepsilon_{\text{ej},\text{final}}$	$\frac{p_{r,\text{ej}}}{M_{\text{cloud}}\sigma}$	$\frac{p_{r,\text{ej}}}{M_*\sigma}$	$\frac{p_{r,\text{ej}}}{M_{\text{ej}}v_{\text{esc}}}$	$\frac{p_{r,\text{ej}}}{M_*}(\text{km s}^{-1})$	$\alpha_{\text{vir},4}^{\text{a}}$
K1	15	0.87	0.12	0.16	0.18	1.4	3.9	1.3
K5	3.0	0.85	0.12	0.16	0.19	1.4	4.1	1.3
K10	1.5	0.81	0.15	0.19	0.23	1.3	4.9	1.1
<b>K20</b>	0.75	0.61	0.34	0.47	0.78	1.4	17	3.3
K30	0.50	0.54	0.44	0.73	1.3	1.7	29	— <sup>b</sup>
K40	0.38	0.51	0.49	0.91	1.8	1.9	38	— <sup>b</sup>
R7.1	0.75	0.70	0.25	0.60	0.87	2.5	22	1.9
<b>R10</b>	0.75	0.61	0.34	0.47	0.78	1.4	17	3.3
R14.1	0.75	0.53	0.39	0.33	0.62	0.86	11	5.2
M0.5	0.75	0.50	0.44	0.41	0.82	0.95	12	2.8
<b>M1</b>	0.75	0.61	0.34	0.47	0.78	1.4	17	3.3
M2	0.75	0.71	0.23	0.52	0.73	2.3	22	1.6
R5M0.25	0.75	0.58	0.36	0.60	1.0	1.7	16	1.5
R7.1M0.5	0.75	0.62	0.33	0.54	0.86	1.7	16	4.0
<b>R10M1</b>	0.75	0.61	0.34	0.47	0.78	1.4	17	3.3
R14.1M2	0.75	0.61	0.36	0.41	0.68	1.2	17	4.8
R20M4	0.75	0.66	0.27	0.35	0.53	1.3	16	1.7

**Note.** — All results are given at time  $t = 8 t_{\text{ff}}$ , except for  $\alpha_{\text{vir},4}$ .

<sup>a</sup> The virial parameter is given at time  $t = 4 t_{\text{ff}}$ .

<sup>b</sup> In runs K30 and K40, the cloud has become unbound by  $t = 4 t_{\text{ff}}$  and the gas density is at the floor value, such that  $\alpha_{\text{vir},4}$  is not longer meaningful.

where  $R_{\text{box}} = L_{\text{box}}/2 = 2R_{\text{cloud}}$  is the distance from the center to the edge of the computational box. In Table 3, we compare  $p_{r,\text{ej}}$  to the product of the total ejected gas mass and this escape speed. We see once again that this ratio is correlated with  $\Sigma$ , the initial surface density of the cloud, and only for the lowest value of  $\Sigma$  considered ( $0.33 \text{ g cm}^{-2}$  in models M0.5 and R14.1) is this ratio less than 1. For all other models, the ratio  $p_{r,\text{ej}}/M_{\text{ej}}v_{\text{esc}}$  is greater than 1, indicating that the bulk of the ejected gas is likely unbound.

#### 4. SUMMARY AND DISCUSSION

In this work, we present the results of a set of numerical RHD simulations of star-forming, turbulent GMCs. We focus on the dynamical effects of reprocessed radiation that originates in massive star clusters, in particular, on the ability of radiation forces to limit further gravitational collapse and destroy the GMC by driving gas outward. Our models investigate conditions and processes similar to those experienced and created by forming SSCs. Our simulations are conducted using the *Hyperion* extension of the *Athena* code; *Hyperion* solves the two-moment RHD equations using the  $M_1$  closure and the RSLA (see SO13). To represent the interaction of IR radiation with the dusty ISM, we adopt the radiative equilibrium condition, such that the absorption and emission of radiation by the fluid are assumed to balance identically everywhere. Star clusters are treated in an idealized manner, with regions of collapsing gas creating sink particles that become local radiation sources. We adopt spatially-uniform opacity and an isothermal equation of state for simplicity, but consider models with a wide range of opacity,  $\kappa = 1 - 40 \text{ cm}^2 \text{ g}^{-1}$ , to test the dependence on this important parameter. We also explore a range of cloud masses and sizes similar to those observed in starburst regions, with initial cloud surface density  $\Sigma = 0.3 - 1.3 \text{ g cm}^{-2}$  (or  $1600 - 6000 M_{\odot} \text{ pc}^{-2}$ ). All models are initiated with a turbulent velocity disper-

sion,  $\sigma$ , such that kinetic and gravitational energy are in equipartition. Table 1 summarizes the input model parameters. While idealized in several respects, to our knowledge this is the first study that has used self-consistent, three-dimensional RHD simulations to investigate the dynamics of IR radiation feedback in cluster-forming turbulent GMCs.

In all of our models, evolution to a final state occurs over several free-fall times (see, e.g., Figure 16). By  $\sim 1 t_{\text{ff}}$ , gravitational collapse leads to the formation of the first star particles, and by  $\sim 2 - 4 t_{\text{ff}}$ , they gain most of the mass they will accrete in their lifetimes. The evolution of gas mass is similar in all models, with the difference that in models with low opacity, essentially all the gas is consumed by star formation, while in models with high opacity, accretion is halted by radiative feedback. For runs with  $\kappa = 1, 5, 10 \text{ cm}^2 \text{ g}^{-1}$  ( $f_{\text{Edd},*} < 1$ ), accretion onto star particles slows after  $\sim 2 t_{\text{ff}}$ ; the surrounding gas maintains a quasi-steady value of the virial parameter  $\sim 1 - 1.5$  over the next  $\sim 6 t_{\text{ff}}$  (Fig. 18), and little additional mass is ejected from the simulation box. For the runs with  $\kappa = 20, 30, 40 \text{ cm}^2 \text{ g}^{-1}$  ( $f_{\text{Edd},*} > 1$ ), the virial parameter diverges after  $\sim 2 - 3 t_{\text{ff}}$ , and most of the remaining gas is ejected from the box.

The most important parameter in determining  $\varepsilon_{*,\text{final}}$ , the net efficiency of star formation over the lifetime of a cloud, is  $f_{\text{Edd},*} \equiv \kappa\Psi/(4\pi cG)$ , where  $\Psi$  is the mean luminosity-to-mass ratio. When  $f_{\text{Edd},*} < 1$ , for  $\kappa < 15 \text{ cm}^2 \text{ g}^{-1}$  (taking  $\Psi = 1700 \text{ erg s}^{-1} \text{ g}^{-1}$ ; see Equation 10), star formation efficiencies are high (exceeding 80%); almost all the mass ejected from the box (at  $t < t_{\text{ff}}$ ) is due to the initial turbulence rather than radiation feedback. When  $f_{\text{Edd},*} > 1$ , efficiencies are lower and decrease as  $f_{\text{Edd},*}$  increases, as shown for the K series in Table 3. Of secondary importance is the cloud surface density  $\Sigma$ ; models with lower  $\Sigma$  have lower  $\varepsilon_{*,\text{final}}$

(see the R and M series in Table 3).<sup>11</sup> Models with high  $\kappa$  and low  $\Sigma$  have  $\varepsilon_{*,\text{final}} \sim 0.5$ .

The value of  $f_{\text{Edd},*}$  is also the discriminant between models that have high vs. low values for the ratio of ejected momentum to stellar mass formed,  $p_{r,\text{ej}}/M_*$  (see Table 3). However, we note that the “high” values ( $p_{r,\text{ej}}/M_* \sim 10 - 40 \text{ km s}^{-1}$ ) are still quite low compared to the momentum/stellar mass from other feedback sources (cf. Ostriker & Shetty 2011); for supernovae, this ratio is  $\sim 3000 \text{ km s}^{-1}$  (see, e.g., Kim & Ostriker 2015). For  $f_{\text{Edd},*} > 1$ , we find that the ejected momentum,  $p_{r,\text{ej}}$  is of order  $\sigma M_*$ . We also find that  $p_{r,\text{ej}}/M_*$  increases with the cloud surface density  $\Sigma$ . On average, gas that is ejected has speed a few times the escape speed of the system.

Our simulations indicate that a large value of  $\kappa$  ( $> 10 \text{ cm}^2 \text{ g}^{-1}$ ) would be required for reprocessed radiation to eject a significant proportion of the mass in a cloud. This value is perhaps unphysically large for IR opacities at Solar neighborhood abundance even for warm dust (see Semenov et al. 2003, for temperature-dependent Rosseland mean opacity), with the implication that reprocessed radiation would not substantially limit star formation in typical Milky Way GMCs. However, for galaxies with metallicities higher than Solar, or in dust-enriched regions, such large opacities are possible. The minimum  $\kappa$  for which feedback limits star formation in our turbulent simulations is consistent with the prediction of an extremely simple model: an isotropic spherical cloud surrounding a central stellar cluster, in which gravity and radiation are the only forces. For this highly idealized situation, Equation (13) shows that the critical opacity for which radiation forces can begin to exceed gravity immediately outside the cluster (preventing further accretion) is  $\kappa_{\text{crit}} = 15 \text{ cm}^2 \text{ g}^{-1} (\Psi/1700 \text{ erg s}^{-1} \text{ g}^{-1})^{-1}$ . In spite of having a similar critical transition, however, the simple spherical model does not describe the detailed functional dependence of the numerical models on  $\kappa$ ; for example, unlike Equation (12), the K series does not show  $\varepsilon_{*,\text{final}} \propto \kappa^{-1}$  at  $\kappa > \kappa_{\text{crit}}$  (when  $f_{\text{Edd},*} > 1$ ).

One difference between the simple spherical model and our turbulent simulations is the anti-correlation between the gas density,  $\rho$ , and the radial flux,  $F_r$  (see Figures 12 and 13). Thus, whereas  $f_{\text{Edd},\text{sph}}(r) \propto f_{\text{Edd},*} \propto \kappa$  for the spherical model (Equation 10), the cumulative  $f_{\text{Edd},\text{cum}}(r)$  (see Equation 15) measured in our simulations is not linear in  $\kappa$  (see Table 2). In our fiducial model, Figure 12 shows that while  $f_{\text{Edd}}(r) < 1$  at most radii,  $f_{\text{Edd},\text{spec}} > 1$  at most radii; this is a consequence of anti-correlation (see Equation 13 and 14). For the K series, the anti-correlation between density and radial flux increases at higher values of  $\kappa$ , and  $f_{\text{Edd},\text{cum}}(r \rightarrow 0)$  remains less than unity for all values of  $\kappa$ . Nevertheless, even when the cumulative Eddington factor is less than unity, some fluid elements become unbound, reducing  $\varepsilon_{*,\text{final}}$  at high enough  $\kappa$ .

<sup>11</sup> We note that the relative sensitivity to  $\kappa$  and relative insensitivity to  $\Sigma$  for the dynamical response of a turbulent, self-gravitating cloud to reprocessed radiation is the opposite of the dynamical response to direct UV radiation from embedded clusters, which strongly depends on  $\Sigma$  (Raskutti, Ostriker, & Skinner 2015, in preparation; see also Fall et al. 2010; Thompson & Krumholz 2014).

Krumholz & Thompson (2012) found, in their 2D RHD simulations of turbulent disks using FLD, that the radiation flux is strongly anti-correlated with the matter distribution. However, the FLD approximation may contribute in part to this result; it is well-known that radiation in this approximation can easily “leak” around dense structures without creating shadows behind them (see, e.g., Hayes & Norman 2003). This question was investigated by Davis et al. (2014), who demonstrated flux-density anti-correlations in turbulent RHD simulations using both FLD and more accurate variable Eddington tensor (VET) methods. They show that the anti-correlation is much stronger using the FLD method compared to their VET method, since the former does not account for the relative insensitivity of the flux to strong density contrasts in filamentary structures when the optical depths across their widths are of order unity or less. Because the  $M_1$  approximation we have adopted does not resolve angular variations in the intensity of radiation and can have difficulty capturing the true radiation field in some situations, it will be important to check the results we have obtained with other more accurate (but more computationally expensive) RHD methods such as VET.

Motivated by analytic spherical models of cluster formation in dusty clouds (Krumholz & Matzner 2009; Murray et al. 2010), current galaxy formation simulations (e.g., Hopkins et al. 2011, 2014; Agertz et al. 2013) have adopted simple subgrid treatments of the force arising from reprocessed IR radiation. In these treatments, the single-scattering UV force,  $L_*/c$ , is boosted via photon trapping by a factor  $\tau_{\text{IR}}$ , the mean optical depth to IR through a cloud. In fact, our comparisons between  $f_{\text{trap},\text{cum}}$  and  $\tau$  (defined in Equations 16 and 17) as shown in Figure 15 and Table 2 indicate that  $\tau L_*/c$  may overestimate the true reprocessed radiation force by a factor of  $\sim 4 - 5$ . First, the force may be reduced due to anti-correlation of the flux and density, as noted above. Second, the assumption of a single, centrally-embedded cluster may be too naïve. A massive cloud may contain several clusters in a distributed configuration, especially at early stages before these can merge. Radiation forces on gas within a cloud with distributed sources is subject to cancellation, and only far from the center of mass of the distribution would the radiation field approach that of a single concentrated source. Meanwhile, the largest contribution to the optical depth may be from the dense central region of the cloud.

In addition to accounting for radiation-matter anti-correlation and distributed radiation sources, it is also important for models that apply IR feedback via a subgrid model to ensure that the inward gravitational forces are consistent with the imposed outward radiation forces. This requires that gravity be spatially and temporally well-resolved within any clouds where radiation forces are applied. If gravity is softened at small scales, then collapse may not occur as rapidly as it realistically should, which would give imposed radiation forces an unphysical advantage. A situation of this kind might help explain why Hopkins et al. (2011) concluded that reprocessed radiation could play a dominant role in regulating star formation (for their “HiZ” model), even though their smooth particle hydrodynamics (SPH) simulations

adopted a value  $\kappa = 5 \text{ cm}^2 \text{ g}^{-1}$  that we found leads to a negligible reduction in a cloud's star formation efficiency – whether for fully turbulent simulations or an idealized spherical system. If limited resolution vitiates the direct action of small-scale gravity in star-forming clouds, then to avoid a gravity/radiation imbalance it would be necessary to incorporate effects of that gravity as part of a subgrid model for effects of radiation. More generally, the limited resolution of galaxy formation simulations precludes direct simulation of many small-scale physical processes, but as feedback is crucial to the control of star formation, application of subgrid treatments is unavoidable. Spatially resolved direct RHD/MHD simulations can be used to identify the most important feedback processes, and to design and calibrate subgrid treatments that capture these key effects.

In the present work, we have focused on the effects of reprocessed IR radiation, with our simulations suggesting that this form of feedback is unlikely to significantly reduce star formation within GMCs unless the dust abundance and opacity are higher than expected for Solar metallicity conditions. Alternatively, since the opacity  $\kappa$  and luminosity-to-mass ratio  $\Psi$  only appear as a product, a top-heavy stellar mass function could increase  $f_{\text{Edd},*}$ , potentially leading to a reduction in the SFE. Turner et al. (2015) present intriguing evidence of both dust self-enrichment and a boosted  $\Psi$  in Cloud D within NGC 5253. Even so, this cloud has estimated SFE  $\sim 0.6$ , similar to the values of  $\varepsilon_{*,\text{final}}$  we obtain in our high  $f_{\text{Edd},*}$  and  $\Sigma \sim 0.33 \text{ g cm}^{-3}$  models.

Finally, we note that the direct UV radiation from young, hot clusters has an advantage over IR in that optical depths become large even when clouds have much lower column densities. Initial study (Raskutti, Ostriker, & Skinner 2015, in preparation) of the effects of (non-ionizing) UV, using RHD models similar to those of this paper, suggests that this direct radiation may be effective in limiting the SFE within low surface density GMCs.

We thank the referee for providing a helpful report. We also thank Taysun Kimm, Chris Matzner, and Jim Stone for helpful comments and suggestions on the manuscript. This work was supported by Grants No. AST-1312006 and PHY-1144374 from the National Science Foundation. MAS is supported by the Max-Planck/Princeton Center for Plasma Physics. Part of this project was conducted during a visit to the KITP at U.C. Santa Barbara, which is supported by the National Science Foundation under Grant No. PHY-1125915. Simulations were performed on the computational resources supported by the PICSciE TIGRESS High Performance Computing Center at Princeton University.

## REFERENCES

- Agertz, O., Kravtsov, A. V., Leitner, S. N., & Gnedin, N. Y. 2013, *ApJ*, 770, 25
- Bertoldi, F., & McKee, C. F. 1992, *ApJ*, 395, 140
- Binette, L., Wilson, A. S., Raga, A., & Storch-Bergmann, T. 1997, *A&A*, 327, 909
- Dale, J. E., Ercolano, B., & Bonnell, I. A. 2012, *MNRAS*, 424, 377
- . 2013, *MNRAS*, 430, 234
- Davis, S. W., Jiang, Y.-F., Stone, J. M., & Murray, N. 2014, *ArXiv e-prints*
- Dobbs, C. L., et al. 2014, *Protostars and Planets VI*, 3
- Dopita, M. A., Groves, B. A., Sutherland, R. S., Binette, L., & Cecil, G. 2002, *ApJ*, 572, 753
- Draine, B. T. 2011a, *ApJ*, 732, 100
- . 2011b, *Physics of the Interstellar and Intergalactic Medium* (Princeton: Princeton University Press)
- Elmegreen, B. G. 1983, *MNRAS*, 203, 1011
- Fall, S. M., Krumholz, M. R., & Matzner, C. D. 2010, *ApJ*, 710, L142
- Federrath, C., & Klessen, R. S. 2012, *ApJ*, 761, 156
- Geen, S., Rosdahl, J., Blaizot, J., Devriendt, J., & Slyz, A. 2015, *MNRAS*, 448, 3248
- Gnedin, N. Y., & Abel, T. 2001, *New A*, 6, 437
- Gong, H., & Ostriker, E. C. 2009, *ApJ*, 699, 230
- . 2011, *ApJ*, 729, 120
- . 2013, *ApJS*, 204, 8
- González, M., Audit, E., & Huynh, P. 2007, *A&A*, 464, 429
- Harper-Clark, E., & Murray, N. 2009, *ApJ*, 693, 1696
- Hayes, J. C., & Norman, M. L. 2003, *ApJS*, 147, 197
- Hockney, R. W., & Eastwood, J. W. 1988, *Computer simulation using particles* (Bristol: Hilger)
- Hopkins, P. F., Kereš, D., Oñorbe, J., Faucher-Giguère, C.-A., Quataert, E., Murray, N., & Bullock, J. S. 2014, *MNRAS*, 445, 581
- Hopkins, P. F., Quataert, E., & Murray, N. 2011, *MNRAS*, 417, 950
- Iffrig, O., & Hennebelle, P. 2015, *A&A*, 576, A95
- Johnson, K. E., & Kobulnicky, H. A. 2003, *ApJ*, 597, 923
- Johnson, K. E., Kobulnicky, H. A., Massey, P., & Conti, P. S. 2001, *ApJ*, 559, 864
- Johnson, K. E., Leroy, A. K., Indebetouw, R., Brogan, C. L., Whitmore, B. C., Hibbard, J., Sheth, K., & Evans, A. S. 2015, *ApJ*, 806, 35
- Kawamura, A., et al. 2009, *ApJS*, 184, 1
- Kepley, A. A., Reines, A. E., Johnson, K. E., & Walker, L. M. 2014, *AJ*, 147, 43
- Kim, C.-G., & Ostriker, E. C. 2015, *ApJ*, 802, 99
- Kobulnicky, H. A., & Johnson, K. E. 1999, *ApJ*, 527, 154
- Krumholz, M. R., & Matzner, C. D. 2009, *ApJ*, 703, 1352
- Krumholz, M. R., McKee, C. F., & Klein, R. I. 2004, *ApJ*, 611, 399
- Krumholz, M. R., & Thompson, T. A. 2012, *ApJ*, 760, 155
- Krumholz, M. R., et al. 2014, *ArXiv e-prints*
- Larson, R. B. 1969, *MNRAS*, 145, 271
- Leisawitz, D., Bash, F. N., & Thaddeus, P. 1989, *ApJS*, 70, 731
- Leitherer, C., et al. 1999, *ApJS*, 123, 3
- Leroy, A. K., et al. 2015, *ApJ*, 801, 25
- Levermore, C. D., & Pomraning, G. C. 1981, *ApJ*, 248, 321
- Lopez, L. A., Krumholz, M. R., Bolatto, A. D., Prochaska, J. X., & Ramirez-Ruiz, E. 2011, *ApJ*, 731, 91
- Lopez, L. A., Krumholz, M. R., Bolatto, A. D., Prochaska, J. X., Ramirez-Ruiz, E., & Castro, D. 2014, *ApJ*, 795, 121
- Martizzi, D., Faucher-Giguère, C.-A., & Quataert, E. 2015, *MNRAS*, 450, 504
- Matzner, C. D. 2002, *ApJ*, 566, 302
- McKee, C. F., & Ostriker, E. C. 2007, *Annual Review of Astronomy and Astrophysics*, 45, 565
- Miura, R. E., et al. 2012, *ApJ*, 761, 37
- Murray, N. 2009, *ApJ*, 691, 946
- . 2011, *ApJ*, 729, 133
- Murray, N., Quataert, E., & Thompson, T. A. 2010, *ApJ*, 709, 191
- Ostriker, E. C., & Shetty, R. 2011, *ApJ*, 731, 41
- Pellegrini, E. W., et al. 2007, *ApJ*, 658, 1119
- Penston, M. V. 1969, *MNRAS*, 144, 425
- Reines, A. E., Johnson, K. E., & Hunt, L. K. 2008, *AJ*, 136, 1415
- Rogers, H., & Pittard, J. M. 2013, *MNRAS*, 431, 1337
- Rosdahl, J., Blaizot, J., Aubert, D., Stranex, T., & Teyssier, R. 2013, *MNRAS*, 436, 2188
- Scoville, N. Z., Polletta, M., Ewald, S., Stolovy, S. R., Thompson, R., & Rieke, M. 2001, *AJ*, 122, 3017
- Semenov, D., Henning, T., Helling, C., Ilgner, M., & Sedlmayr, E. 2003, *A&A*, 410, 611
- Skinner, M. A., & Ostriker, E. C. 2013, *ApJS*, 206, 21
- Stone, J. M., & Gardiner, T. 2009, *New A*, 14, 139
- Stone, J. M., Gardiner, T. A., Teuben, P., Hawley, J. F., & Simon, J. B. 2008, *ApJS*, 178, 137

- Stone, J. M., Ostriker, E. C., & Gammie, C. F. 1998, *ApJ*, 508, L99
- Thompson, T. A., & Krumholz, M. R. 2014, *ArXiv e-prints*
- Thompson, T. A., Quataert, E., & Murray, N. 2005, *ApJ*, 630, 167
- Townsley, L. K., Feigelson, E. D., Montmerle, T., Broos, P. S., Chu, Y.-H., & Garmire, G. P. 2003, *ApJ*, 593, 874
- Truelove, J. K., Klein, R. I., McKee, C. F., Holliman, II, J. H., Howell, L. H., & Greenough, J. A. 1997, *ApJ*, 489, L179
- Tsai, C.-W., Turner, J. L., Beck, S. C., Meier, D. S., & Ho, P. T. P. 2009, *AJ*, 137, 4655
- Turner, J. L., Beck, S. C., Benford, D. J., Consiglio, S. M., Ho, P. T. P., Kovács, A., Meier, D. S., & Zhao, J.-H. 2015, *Nature*, 519, 331
- Turner, J. L., Beck, S. C., & Ho, P. T. P. 2000, *ApJ*, 532, L109
- Turner, J. L., Ho, P. T. P., & Beck, S. C. 1998, *AJ*, 116, 1212
- Walch, S. K., & Naab, T. 2014, *ArXiv e-prints*
- Walch, S. K., Whitworth, A. P., Bisbas, T., Wünsch, R., & Hubber, D. 2012, *MNRAS*, 427, 625
- Whitmore, B. C., et al. 2014, *ApJ*, 795, 156
- Yeh, S. C. C., & Matzner, C. D. 2012, *ApJ*, 757, 108



## APPENDIX

## FOURIER TRANSFORM POISSON SOLVER WITH OPEN BOUNDARY CONDITIONS

Equation (5) may be rewritten as a discrete convolution over the simulation domain  $[0, L_x] \times [0, L_y] \times [0, L_z]$ , divided into  $N_x N_y N_z$  equal zones. Letting  $(a, b, c)$  and  $(a', b', c')$  represent zone-center integer indices, we may define the Green function kernel  $\mathcal{G}(x_a, y_b, z_c; x_{a'}, y_{b'}, z_{c'}) = \mathcal{G}(|x_a - x_{a'}|, |y_b - y_{b'}|, |z_c - z_{c'}|) = \mathcal{G}(|a - a'| \Delta x, |b - b'| \Delta y, |c - c'| \Delta z)$  as a symmetric function on an extended domain  $[-L_x, L_x] \times [-L_y, L_y] \times [-L_z, L_z]$  or equivalently  $[-N_x, N_x - 1] \times [-N_y, N_y - 1] \times [-N_z, N_z - 1]$ . We also extend  $\rho(x_a, y_b, z_c)$  over the larger domain, setting the value to zero for  $a < 0$ ,  $b < 0$ , or  $c < 0$ . Equation (5) then becomes

$$\begin{aligned} \Phi(x_a, y_b, z_c) = & G \sum_{a'=-N_x}^{N_x-1} \sum_{b'=-N_y}^{N_y-1} \sum_{c'=-N_z}^{N_z-1} \\ & \times \mathcal{G}(x_a, y_b, z_c; x_{a'}, y_{b'}, z_{c'}) \\ & \times \rho(x_{a'}, y_{b'}, z_{c'}) \Delta x \Delta y \Delta z. \end{aligned} \quad (\text{A1})$$

Taking both  $\mathcal{G}_{ijk}$  and  $\rho_{ijk}$  to be  $2N_x$ -,  $2N_y$ -, and  $2N_z$ -periodic sequences in the indices  $i, j$ , and  $k$ , respectively, and using the discrete analog of the Fourier Convolution Theorem, it follows from Equation (A1) that

$$\begin{aligned} \Phi_{ijk} = & \frac{G}{(2N_x)(2N_y)(2N_z)} \sum_{l=0}^{2N_x-1} \sum_{m=0}^{2N_y-1} \sum_{n=0}^{2N_z-1} \\ & \times \hat{\mathcal{G}}_{lmn} \hat{\rho}_{lmn} \\ & \times \exp \left[ -2\pi i \left( \frac{il}{2N_x} + \frac{jm}{2N_y} + \frac{kn}{2N_z} \right) \right], \end{aligned} \quad (\text{A2})$$

where  $\hat{\mathcal{G}}_{lmn}$  and  $\hat{\rho}_{lmn}$  are the respective discrete Fourier transforms (DFTs) of the sequences  $\mathcal{G}_{ijk}$  and  $\rho_{ijk}$ . This method is computationally efficient since the DFTs can be computed via FFTs.

In this work, we compute  $\hat{\mathcal{G}}_{lmn}$  directly via the DFT of the periodic sequence

$$\begin{aligned} \mathcal{G}_{ijk} = & - \left\{ [(i \bmod 2N_x) \Delta x]^2 \right. \\ & + [(j \bmod 2N_y) \Delta y]^2 \\ & \left. + [(k \bmod 2N_z) \Delta z]^2 \right\}^{-1/2}, \end{aligned} \quad (\text{A3})$$

where we set  $\mathcal{G}_{000} = 0$  to avoid dividing by zero. The DFT is computed once and stored. An alternative to this approach is to use the DFT obtained from the finite-difference approximation to the Laplace equation,

$$\begin{aligned} \hat{\mathcal{G}}_{lmn} = & 2\pi \left\{ \frac{\cos(\pi l / N_x) - 1}{\Delta x^2} \right. \\ & + \frac{\cos(\pi m / N_y) - 1}{\Delta y^2} \\ & \left. + \frac{\cos(\pi n / N_z) - 1}{\Delta z^2} \right\}^{-1}, \end{aligned} \quad (\text{A4})$$

(see the Appendix of Gong & Ostriker 2013), where once again we set  $\hat{\mathcal{G}}_{000} = 0$ . The approach we adopt here is more accurate for long-range forces compared to the result in Equation (A4), although it does not have a closed-form analytic expression, and therefore must be stored in an array of size  $8N_x N_y N_z$ .